Environmental Science & Technology

ARTICLE

pubs.acs.org/est

Metallothionein-Like Multinuclear Clusters of Mercury(II) and Sulfur in Peat

Kathryn L. Nagy,*[,†] Alain Manceau,[‡] Jarrod D. Gasper,[§,⊥] Joseph N. Ryan,[∥] and George R. Aiken[§]

[†]Department of Earth and Environmental Sciences, MC-186, 845 West Taylor Street, University of Illinois at Chicago, Chicago, Illinois 60607, United States

[‡]ISTerre-Maison des Géosciences, CNRS and Université J. Fourier, BP 53, 38041 Grenoble Cedex 9, France

[§]United States Geological Survey, Water Resources Discipline, 3215 Marine Street, Boulder, Colorado 80303, United States

[∥]Department of Civil, Environmental, and Architectural Engineering, University of Colorado Boulder, 428 UCB, Boulder, Colorado 80309-0428, United States

Supporting Information

ABSTRACT: Strong mercury(II)−sulfur (Hg-SR) bonds in natural organic matter, which influence mercury bioavailability, are difficult to characterize. We report evidence for two new Hg-SR structures using X-ray absorption spectroscopy in peats from the Florida Everglades with added Hg. The first, observed at a mole ratio of organic reduced S to Hg (S_{red}/Hg) between 220 and 1140, is a Hg_4S_x type of cluster with each Hg atom bonded to two S atoms at 2.34 Å and one S at 2.53 Å, and all Hg atoms 4.12 Å apart. This model structure matches those of metal−thiolate clusters in metallothioneins, but not those of HgS minerals. The second, with one S atom at 2.34 Å and about six C atoms at 2.97 to 3.28 Å, occurred at S_{red}/Hg between 0.80 and 4.3 and suggests Hg binding to a thiolated aromatic unit. The multinuclear Hg cluster indicates a strong binding environment to cysteinyl sulfur that might impede methylation. Along with a linear $Hg(SR)_2$ unit with Hg—S bond lengths of 2.34 Å at S_{red}/Hg of about 10 to 20, the new structures support a continuum in Hg-SR binding strength in natural organic matter.

INTRODUCTION

Reduced sulfur (S_{red}) ligands are the main pool of strong binding sites for mercury(II) (Hg) in natural organic matter (OM) that may influence methylation rates, distribution and transport, and ecotoxicity of mercury. The S_{red} derives from biomolecules produced by organisms, free sulfide species formed during microbial sulfate reduction, and recycled products of OM degradation and diagenesis. Total amounts of S_{red} in OM range typically from about 0.1−2 wt %, sufficient to bind even unusually high concentrations of Hg.

Small organic and inorganic Hg−S_{red} species can enable methylation,[1,2] but effects of Hg bound to larger OM molecules on microbial methylation and direct toxicity to fish and filter-feeders are ambiguous or unknown.[3−5] Unlike small biomolecules, which are labile and can rapidly exchange thiol-bonded Hg,[6] macromolecular OM may have binding environments that are influential in decreasing bioavailability of Hg. Because peat and soil OM contain more macromolecular plant-derived compounds, as well as more reduced and total S, compared to dissolved OM (DOM), they may sequester Hg from the aqueous phase.

The binding strength of Hg to OM, expressed as conditional $HgLR^+$ and HgL_2R formation constants, spans from about 10^{10} to 10^{38},[7−14] corresponding to mole ratios of S_{red} to bound Hg (S_{red}/Hg) from less than 1 to about 77000 in the solid phase at equilibrium with dissolved mercury. In the form $Hg(LR)_2$ the largest constants are $\geq 10^{43}$, matching values for thiol-binding in low molecular weight organic molecules.[15] The strongest binding sites containing S_{red} are fewer in number than the markedly weaker sites containing O and/or N.[8]

Binding constants must be linked to molecular structures to quantify reactions between OM and Hg species. Such structures have been characterized in peat, soil OM, and humic acid with added metal using extended X-ray absorption fine-structure (EXAFS) spectroscopy. At mole ratios of S_{red}/Hg = 0.3 to 1.2 a structure with one S and one O or N bond (i.e., R(O/N)HgSR) was observed[16,17] whereas at S_{red}/Hg = 1.6 to 4, 60 to 90% of added Hg bonded to 1.3 to 1.7 S atoms, suggesting up to 70% $Hg(SR)_2$ in a linear configuration.[17] At S_{red}/Hg = 20 to 100 a $Hg(SR)_{2-3}$ complex with two S ligands at 2.34 Å and a tentative third near 3 Å in a T-shape geometry was reported.[18,19] Possible three-coordinate binding is supported by the average release of 2.7 protons for each adsorbed Hg atom in peat humic acid at S_{red}/Hg = 120.[13]

Peat typically contains about 0.1 ppm Hg (0.1 mg Hg/kg OM, equivalent to about 10^6 mol S_{red}/mol Hg). This amount of

Received: March 27, 2011
Accepted: July 14, 2011
Revised: July 12, 2011
Published: August 02, 2011

mercury is about 1% of the adsorbed amount (10 ppm Hg) at which the strongest binding constants in OM have been measured,[8,9,12] and about 0.1% of the lowest value at which EXAFS spectra are measurable today. Because only about 0.02% of S_{red} is needed to bind 0.1 ppm Hg, molecular structures identified by EXAFS at around 100 ppm Hg, or about 20% of the S_{red}, may reasonably approximate the strongest sites. Our goal was to distinguish binding environments that involved S_{red} by obtaining and interpreting EXAFS spectra of Hg-containing peats, including spectra obtained at liquid He temperature.

The peats were collected from two locations (F1 and 2BS) in the Everglades that had different inorganic sulfide (HS^-) concentrations and Hg methylation rates.[20] They were shown to have dominantly strong to weak binding at adsorbed Hg concentrations over the range of 1−400000 ppm.[9] We observed two new molecular binding environments out of a total of four between 59 and 99100 ppm added Hg (S_{red}/Hg mole ratio from 1140 to 0.50) that expand our understanding of how the continuum of sulfur binding sites in OM may form and influence bioavailability of mercury.

EXPERIMENTAL SECTION

We adsorbed mercury to the peats using the experimental procedure described previously[9] except that the concentration of peat was 10 times higher (0.1 g peat in 0.25 L of solution) to obtain enough material for EXAFS spectroscopic analysis. Experiments were conducted at initial solution concentrations of mercury from 3×10^{-7} to 2×10^{-4} mol/L. Mercury was analyzed using cold vapor atomic fluorescence spectroscopy (PS Analytical Ltd., Kent, UK).

EXAFS spectra at the Hg-L_3 edge were recorded at room temperature (RT) and nine months later at liquid helium temperature (He-T; 8−16 K) at beamline BM30B (FAME) of the European Synchrotron Radiation Facility (ESRF) and analyzed by standard techniques. X-ray absorption near-edge structure (XANES) spectra at the S-K edge were recorded on unreacted peat at RT at beamline 10.3.2, Advanced Light Source (ALS). Fractional abundances of reduced and oxidized sulfur species were obtained by linear combination fitting of reference spectra. Binding structures for Hg were identified by comparing spectral features of samples to those of reference compounds, fitting sample spectra with linear combinations of spectra, and modeling Fourier-transformed k^3-weighted spectra using amplitude and phase shift functions calculated from first principles.

Details of the experiments and analyses are in the Supporting Information (SI).

RESULTS AND DISCUSSION

In contrast to the generally linear trend in the adsorption isotherms, which may be explained by at most two binding sites, the EXAFS spectral analysis revealed four structural binding environments, three of which involved sulfur ligands. Two of the binding environments identified are reported for the first time. One is a multinuclear Hg-SR coordination structure observed at low amounts of adsorbed Hg and the other is indicative of Hg bonded to thiolated aromatic subunits observed at high amounts of adsorbed Hg. We first present results for the adsorption isotherms and XANES spectra of the sulfur speciation in the peats, followed by results for the individual binding environments derived from the EXAFS spectra.

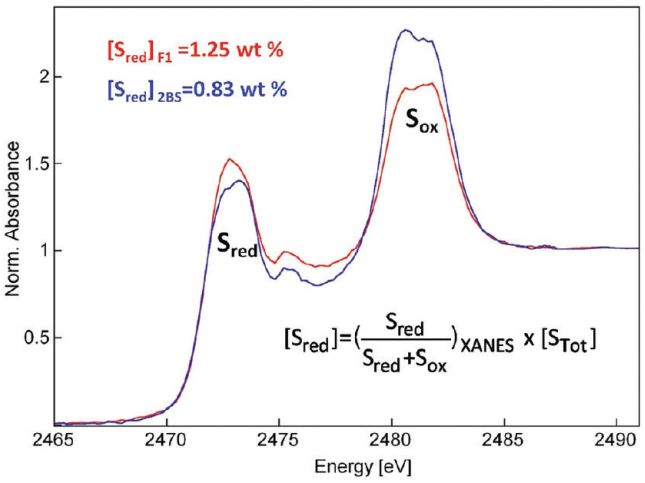

Figure 1. S-XANES spectra for F1 and 2BS peats. The peats were fit with approximately the same amounts of cystine (29−31%), sulfoxide (9−11%), and sulfate (6−7%), but F1 had more cysteine (41 vs 34%) and 2BS more sulfonate (23 vs 16%). The first difference is seen in the ratio of the peak amplitudes of reduced (S_{red}) to oxidized sulfur (S_{ox}), which is higher for F1 than 2BS, and the second in the asymmetrical shape of the oxidized sulfur peak for 2BS which crests at the energy of the sulfonate component (2480.5 eV).

S-XANES Spectra and Adsorption Isotherms. Initial values of the mole ratio S_{red}/Hg in the peats were 3×10^5 for 2BS and 8×10^5 for F1, where S_{red} was determined by XANES spectroscopy (Figure 1 and SI). The peats adsorbed 1 to 99100 ppm Hg (S_{red}/Hg = 78300 to 0.50, respectively) as aqueous Hg concentration increased, similarly to earlier observations[9] (SI). At low aqueous concentrations of Hg the F1 peat, which had more total and reduced S (1.79 wt % S_{Total}; 1.25 wt % S_{red}), adsorbed slightly more Hg than the 2BS peat (1.27 wt % S_{Total}; 0.83 wt % S_{red}). One inflection point between 10^{-8} and 10^{-7} mol Hg/L indicates the data might be fit with two Langmuir isotherms representing two binding sites.

EXAFS Spectra at Room Temperature. The k^3-weighted spectra of peats with 59−99100 ppm Hg (S_{red}/Hg = 1140 to 0.50) obtained at RT have features that differentiate three binding environments (Figure 2a). Two are evident by isosbestic points for samples having 4170 to 99100 ppm Hg, resulting from a rightward shift in oscillation frequency and a decrease in amplitude with increasing Hg concentration (Figure 2b). These features show that, with decreasing S_{red}/Hg mole ratio, Hg binding transitions from dominant longer bonds (short wave frequency) with S atoms to shorter bonds (long wave frequency) with atoms of smaller ionic radii (O, N).[17,18]

At any amount of Hg, the F1 spectrum is shifted slightly left of the 2BS spectrum to the point that F1-99 (99100 ppm) is more like 2BS-19 (19000 ppm) than 2BS-99 (99100 ppm). The systematic shift is related to the 50% more S_{red} in the F1 peat and confirms the significance of Hg−S bonds in the EXAFS signal even at high amounts of adsorbed Hg (i.e., low values of S_{red}/Hg).[16,17]

A third binding environment is indicated at lower Hg concentrations by slight leftward shifts of the oscillations, which imply even longer bonds (Figure 2c). This observation motivated measurements at He-T of six samples representing the variation in RT spectra and the spread of S_{red}/Hg values. Freezing slows the thermal motion of atoms, and for an

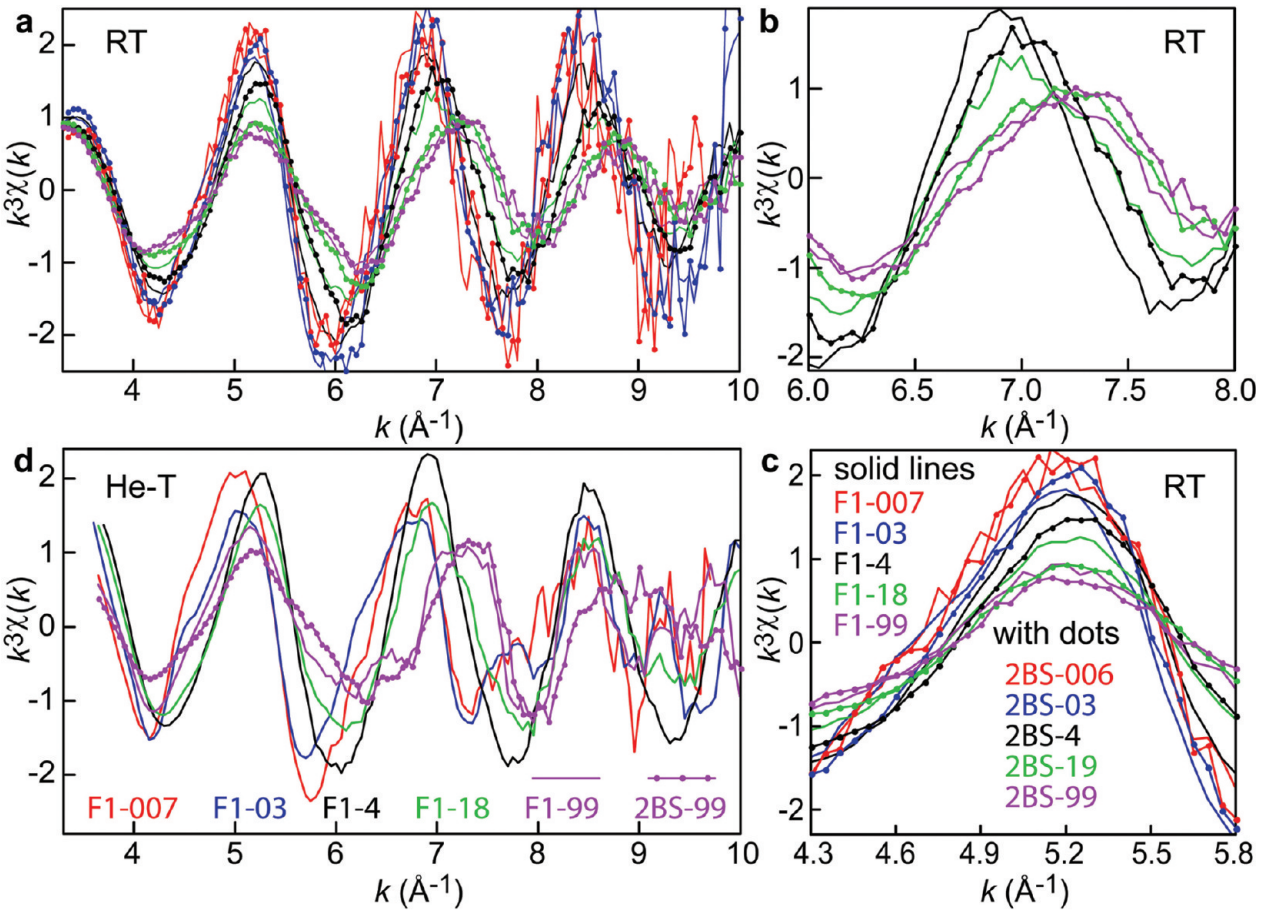

Figure 2. EXAFS spectra for F1 and 2BS peat samples. Sample code suffixes represent adsorbed Hg in ppm (mg Hg/kg peat): −006 and −007 (59 and 69 ppm); −03 (~350 ppm); −4 (~4100 ppm); −18 and −19 (18400 and 19000 ppm); −99 (99100 ppm) (SI). (a) Room temperature (RT) spectra cut at $k = 10$ Å^{-1} for clarity except for −006 and −007 spectra which were stopped at $k = 9.8$ Å^{-1} because of interfering absorbance at the Se K-edge. (b) RT spectra at $k = 6$ to 8 Å^{-1} showing rightward shift to lower frequency at higher Hg concentration, signifying shorter Hg-ligand distances. Spectra at 59 to 350 ppm are omitted for clarity. (c) RT spectra at $k = 4.2$ to 5.6 Å^{-1} showing leftward shift to higher frequency at lower Hg concentration, signifying longer Hg-ligand distances. (d) Spectra at liquid helium temperature (He-T) cut to $k = 10$ Å^{-1}.

individual bond increases the amplitude of the EXAFS signal. Thus, we expected an improved signal-to-noise ratio and better resolution of interatomic distances at liquid He temperature.

EXAFS Spectra at Liquid He Temperature. At He-T, longer Hg—S bonds were more evident by the farther leftward shift of spectra at low Hg concentrations and sinistral asymmetry of the first two oscillations (Figures 2d and 3a). Other bonds, also more apparent at He-T, caused extra small oscillations at about $k = 7.8$ and 9.2 Å^{-1} in F1-007 (69 ppm Hg; S_{red}/Hg = 1140) and F1-03 (353 ppm Hg; S_{red}/Hg = 220) (Figure 2d) and also at 10.6 and 12 Å^{-1} in F1-03 (SI). Detailed analyses of the spectra and modeled coordination structures from low to high adsorbed Hg concentrations (i.e., high to low mole ratios of S_{red}/Hg) are presented below.

Multinuclear Hg—S Binding at Low Hg Concentration. The spectra of F1-03 and F1-007 changed the most between RT and He-T, implicating dominant soft metal-soft ligand Hg—S bonds. Fourier transforms of the F1-03 spectra show that (1) the peak at $R + \delta \approx 2$ Å (distance uncorrected for phase shift) with a small shoulder on the right at RT split into two peaks at about 1.8 and 2.3 Å and (2) the peak at about 4 Å increased in amplitude at He-T (Figure 3a). These changes are understood by comparison to the changes in cinnabar (α-HgS) spectra between RT and He-T (Figure 3b).

At RT the spectrum of α-HgS is dominated by the signal from Hg—S bonds of length 2.38 Å ($R + \delta \approx 2$ Å); the signal from Hg—Hg pairs at $R + \delta \approx 4$ Å is weak. At He-T the signal amplitude is higher and the local structure of α-HgS fully agrees with crystallographic data. Longer Hg—S bonds at 3.07 and 3.26 Å are detected, modeling shows two distinct Hg—Hg pairs at 3.79 Å and 4.11 Å, and longer Hg—Hg pairs at 5.67 and 6.82 Å appear (SI). Similar spectral features are seen in cinnabar spectra obtained at 77 K[21] (SI).

Changes for the F1 peats with temperature, although similar, are distinct from those for cinnabar. Differences include the out-of-phase patterns between $k \approx 10.2$ and 12.8 Å^{-1} and the peak shapes at $R + \delta \approx 4$ Å at He-T. Using the cinnabar spectrum at He-T to guide bond assignments, two Hg—S bonds of length 2.34 Å and one of length 2.53 Å were derived from the F1-03 peat spectrum at He-T along with one Hg—C or Hg—S bond at 3.25 Å, and three Hg—Hg pairs at 4.12 Å (Figure 4a, SI). The counterintuitive weakening of spectral amplitude at low k values in F1-03 at He-T compared to RT is a result of the relative difference in enhancement of amplitude of the two Hg—S bonds at low temperature (SI).

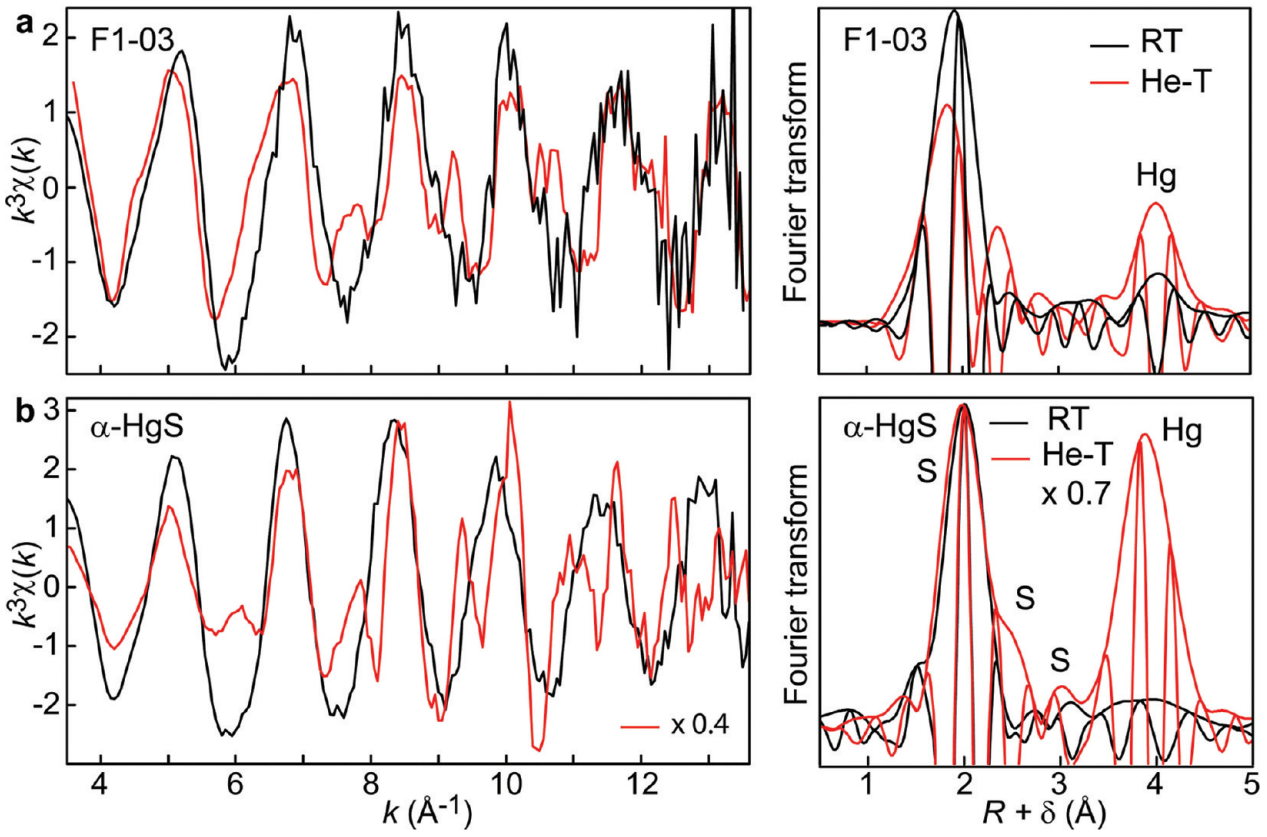

Figure 3. EXAFS spectra (left) and Fourier transforms (right) for F1−03 peat (353 ppm Hg) and cinnabar (α-HgS). Imaginary parts of the Fourier transforms show that the differences in the EXAFS frequencies observed in *k*-space at RT and He-T come from the magnification at low temperature of distant Hg—S and Hg—Hg pairs. (a) F1-03 at RT and He-T. (b) α-HgS at RT and He-T. Amplitudes for the spectra and Fourier transforms of α-HgS were reduced by multiplicative factors to aid comparison of peak shapes and positions.

Comparison of the Hg-SR structure in the peat and metacinnabar (*β*-HgS) at He-T is also warranted, but is not straightforward. Although the spectra for metacinnabar and cinnabar (α-HgS) are distinct at RT, the spectrum of *β*-HgS is similar to that of cinnabar (α-HgS) at He-T, indicating that the structure of the metastable mercuric sulfide (*β*-HgS) approaches that of cinnabar (α-HgS) near absolute zero (SI). Such a structural transition is consistent with the relative thermodynamic stability of the two phases: metacinnabar is the stable phase at higher temperature.[22] The transition is also consistent with a reduction in crystallographic symmetry from cubic (*β*-HgS) to trigonal (α-HgS) as temperature is lowered. A similar transition was reported recently for magnetite which changed structure from cubic to monoclinic at about 125 K.[23] The spectrum of the structurally transformed metacinnabar does not match that of F1-03 at He-T (SI).

We used the bond distances derived for F1-03 at He-T as initial conditions for modeling the RT F1-03 spectrum. A good fit was obtained with two S atoms at 2.35 Å, 0.6 S at 2.57 Å, and 1.6 Hg at 4.14 Å (SI); the 3.25 Å distance was not detected. Like for cinnabar, fewer longer Hg—S and Hg—Hg distances were revealed at RT than at He-T, but none changed significantly (SI). In addition, F1-03 does not match either metacinnabar, which has all Hg—S bonds at 2.51 Å, or cinnabar at RT (SI). Freezing did not change the unique binding between Hg and S in the peat: the multinuclear Hg-SR structure, which is nanosized and surrounded by a relatively flexible organic matrix, is stable.

Organic materials are commonly examined in the frozen state by EXAFS spectroscopy to avoid formation of free radicals that cause photoreduction.[24,25] However, there is virtually no evidence for degraded RT structures during synchrotron measurements of Hg binding to OM,[16−18] likely in part because of the strong bonds that form between Hg and S_{red}. In fact, the small oscillation near 7.8 $Å^{-1}$ at He-T in F1-007 and F1-03 (S_{red}/Hg = 1140 and 220) caused by Hg−Hg pairs is also perceptible in RT spectra of soil OM at S_{red}/Hg = 100 and 20.[18] This is not only further evidence against photoreduction of strongly bound Hg at RT but also supports the conclusion that freezing did not induce the multinuclear structure.

The features of Hg−Hg pairs observed in the He-T spectra of the peats may be visible in the spectra of soil OM at RT[18] because the experimental soil OM−Hg solutions equilibrated for 1 wk[18] compared to 15 h in the peat OM-Hg solutions. Mercury atoms could have had time to move to higher affinity protein-like S_{red} sites even though the soil OM had 75% less S_{red} than the Everglades peats. A similar kinetic effect may have contributed to visualizing the longer bond distances in our He-T analyses given the nine-month interval between the measurements at the two temperatures. In addition, the greater amount of S_{red} in the peats may have accelerated the change in binding enough to detect the multinuclear cluster in the modeled RT spectra despite the short equilibration time. The final pH of our peat experiments was 5−6 vs a pH near 4 for the soil OM.[18] If apparent pK_a values of thiols in peats are in the range of those for plant

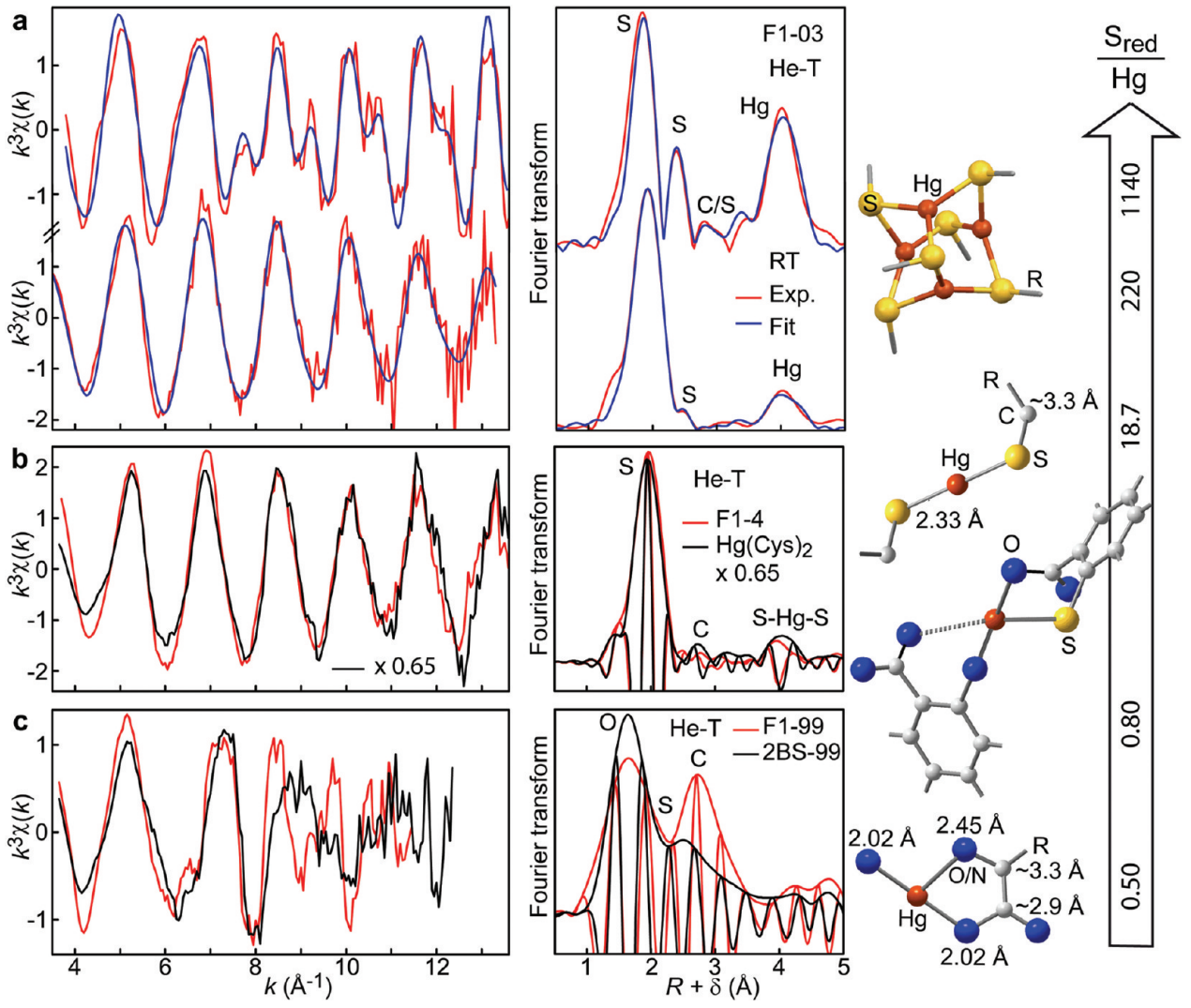

Figure 4. EXAFS spectra, Fourier transforms, and model structures of dominant Hg binding structures (left to right) and correspondence with S_{red}/Hg in the peats (far right). (a) F1−03 (353 ppm Hg) at RT and He-T with model fits. Schematic multinuclear Hg_4S_x structure is at right. Data analysis shows that the Hg—S distance at 2.53−2.57 Å contributes to the right tail of the first peak (SI). Imaginary parts of the Fourier transforms were omitted for clarity. (b) F1-4 (~4100 ppm Hg) and $Hg(Cys)_2$ reference solution at He-T. The modeled $Hg(SR)_2$ structure is shown at the upper right. (c) F1-99 (99100 ppm) and 2BS-99 (99100 ppm) at He-T. A schematic of the five-membered (O,N) chelate ring structure in 2BS-99 is shown at the lower right. Modeled bond distances and coordination numbers in F1-99 suggest the hypothetical structure linking Hg to aromatic rings at the upper right. Atoms coded as oxygen are indistinguishable from nitrogen.

metallothioneins,[26] then accelerated binding of Hg in the peat also could be explained by more deprotonated sites at higher pH.

Similarity of Multinuclear Hg−S Structure to Metal−Thiolate Clusters in Metallothionein Proteins. The average Hg−S structure can be described as a tetrameric cluster (Hg_4S_x) in which three-coordinate molecular units of one Hg atom with two short bonds (2.34 Å) and one longer bond (2.53 Å) to S atoms are arranged so that any two Hg atoms are about 4.12 Å apart (Figure 4a). The bonds around any Hg atom form a Y-shape,[19] precluding successful modeling of the peak at $R + \delta \approx 4$ Å in the Fourier transforms at both temperatures as multiple-scattering from a linear $Hg(SR)_2$ complex[18] (SI). At least 0.5 mol % of S_{red} must be in the cluster, similar to the 0.15−1% deduced for strong binding constants of Hg in other OM samples.[8,9,15]

The Hg_4S_x model cluster resembles polynuclear-thiolate clusters in Cu(I) metalloproteins and metal-peptide compounds.[27] $Cu(I)_4S_6$-type structures with three-coordinate metal centers occur in metallochaperone and metallothionein (MT) proteins with CXC (CysXaaCys) amino acid consensus sequences from mammals and yeast.[28−32] These structures mimic organometallic $[Cu_4(SPh)_6]^{2-}$, which contains thiolated aromatics.[33]

Structures of Hg metalloproteins are few and varied. One three-coordinate unit with Hg—S bond length of 2.43(2) Å was observed in the merR-regulatory protein,[34] and one with either two 2.34 Å and one 2.47 Å or three 2.39 Å Hg—S bonds in a de novo Hg(II)-metalloprotein.[35] In Hg_7-MT, Hg is bonded to either two S atoms at 2.33(2) Å (and possibly two other S at 3.4 Å)[36] or to three S at 2.42(2) Å,[37] whereas in Hg_{18}-MT Hg is bonded to two S atoms at 2.42(3) Å and one Cl at 2.57 Å;[36] no Hg−Hg distances were reported for either Hg-MT. The crystal structure of the metallochaperone Hah1 in the presence of Hg has a distorted tetrahedral coordination with one Hg bonded to

one S at 2.3 Å, two S at 2.5 Å, and one S at 2.8 Å.[38] One Hg atom is thought to bind to two Hah1 molecules each with CXXC sequences. Molecules with CXXC sequences usually form two-coordinate structures as in the MerP Hg(II) transport protein.[39] Three-coordinate binding in a multinuclear cluster was inferred for Hg-loaded MT from *Cicer arietinum* (chickpea) using UV-vis spectroscopy.[40]

$Hg(SR)_2$, Chelate Ring, and Thiolated Aromatic Structures at Higher Hg Concentrations. A linear $Hg(SR)_2$ structure was dominant in the F1-4 peat with 4180 ppm Hg (S_{red}/Hg = 18.7). This structure has the same shorter Hg—S bonds (2.33 Å at He-T and 2.35 Å at RT) as the cluster, but not the longer Hg—S bond (2.53 Å) and Hg−Hg distance (4.12 Å): there is neither a spectral shift to lower k nor extra oscillations at higher k (Figure 4b). The spectrum and Fourier transform at He-T match those for our 1:2 Hg-cysteine solution ($Hg(Cys)_2$), and similarly frozen Hg-cysteine solids,[41] and Hg-cysteine and Hg-glutathione solutions.[41,42] Linearity is confirmed by the peak at $R + \delta \approx 4$ Å in the Fourier transform at He-T, caused by multiple scattering paths (SI). Only 65% of the $Hg(Cys)_2$ spectrum is needed to match the F1−4 spectrum indicating that at least 20−25% of the Hg is bonded to O and/or N (Figure 4b).

The other sample having a dominant binding environment was 2BS-99 (99100 ppm Hg and S_{red}/Hg = 0.50). The spectra indicate shorter bonds between Hg and lower Z atoms (Figures 2 and 4c). In the best model, Hg bonds to one O atom at 2.02 Å, one O or N atom at 2.45 Å, one C atom at 2.87 Å, and one C atom at 3.28 Å (SI). The structure is likely a five-membered chelate ring with one carboxylate O and amino N (α-HN_2) or alcohol O (α-OH) from an α-substituted carbon, similar to structures for monomethylmercury binding to amino acids[43,44] and for Hg and Cu(II) complexed to soil OM and humic acid.[18,24]

The second new Hg−S structure appeared in F1-99 (also having 99100 ppm Hg, but a higher S_{red}/Hg of 0.80 compared to 2BS-99). A small oscillation at about 6.7 $Å^{-1}$ and the shift of the third oscillation at 8 $Å^{-1}$ in the He-T spectrum are distinctive (Figure 4c). The best model gives an average structure around Hg of one O or N atom at 2.02 Å, 0.4 S atoms at 2.34 Å, two C atoms at 2.97 Å, and four C atoms at 3.28 Å (SI). The number of C atoms along with S suggests the presence of thiolated aromatic units.[45] However, the low amount of S indicates that this structure is mixed mainly with the (O,N) chelate ring seen in 2BS-99.

The spectra of F1-18 (18400 ppm Hg; S_{red}/Hg = 4.3) could not be modeled successfully from first principles because there was no dominant binding environment. Instead, RT and He-T spectra were analyzed by linear combination fitting using spectra from the other peat samples. Sample F1-18 has about 67% F1-4 type bonds and 33% of the mixture of bonds modeled in F1-99 (SI), further supporting a continuum in binding environments.

Environmental Implications. As the concentration of adsorbed Hg increased, the Hg atoms filled increasing amounts of progressively weaker binding sites. Binding of highest to lowest affinity corresponds in order to the Hg_4S_x cluster, linear $Hg(SR)_2$, thiolated aromatic, and five-membered chelate ring sites (Figure 4). The first three reinforce the importance of thiolate ligands even at relatively low values of S_{red}/Hg, where OH and N ligands are in great excess. Other relatively weak binding sites with O and N ligands may exist at low values of S_{red}/Hg, but could not be distinguished in this study. Also, the EXAFS spectroscopic data obtained here cannot be used to differentiate O from N ligands such as the imidazole component of histidine which can bind metals in protein structures.[46] A four-coordinate Hg-SR structure like that observed, for example, in the HgHah1 metallochaperone protein[38] or the $Hg(Cys)_4$ species in Hg-cysteine solutions with $H_2Cys/Hg(II) > 5$[41] might form at higher values of S_{red}/Hg than investigated here. However, the longer bond-length expected for such a structure[19] was never dominant in the peat samples.

Thiols may be incorporated into OM as components of biomolecules such as metallothioneins and phytochelatins. Metallothioneins, which have high contents of cysteinyl thiols, are produced by bacteria and eukaryoa and possibly by archaea.[26,47,48] Photosynthetic organisms also produce phytochelatins, which are glutathione-based peptides with (γ-Glu-Cys)$_n$Gly (PC_n, n = 2−11). In addition, thiols can be formed when hydrogen sulfide, typically generated by bacterial sulfate reduction,[49−51] adds to unsubstituted double bonds in alkenes and aromatics from tannins, lignins, and terpenoids.[52,53]

Reduced sulfur in the peats has XANES character like that of thiols in cysteine and disulfide bridges in cystine (SI); that is, the reduced sulfur that forms metal−thiolate clusters in metalloproteins. Such clusters typically have 2−11 metal centers[54] with evidence in bacterial, animal, and plant MTs that histidine residues stabilize the negative charge of the cluster.[55] Histidine residues can also be part of the coordination structure.[46] Values equal to 2−2.7 observed for the ratios of protons exchanged for low amounts of adsorbed Hg in DOM and soil OM at pH ≤ 7[10,13] imply x = 8−11 in the Hg_4S_x structure, in the range of typical numbers of S atoms in MT metal−thiolate clusters.

Living organisms can control the binding of metals to stable clusters in MTs by cellular redox reactions [56,57] and rapid metal exchange can occur through protein folding and unfolding.[58] Metal−thiolate clusters in plant MTs tend to be somewhat less stable than those in most vertebrate MTs at comparable pH,[26,59] which may be related to fewer cysteine residues and longer linker chains between domains in plant MTs. Upon cellular death, metal−thiolate clusters might become incorporated in OM whereas amino acid linker segments likely decompose.

Mercury(II) binds more strongly than Cu(I), Cd(II), Pb(II), and Zn(II) to MTs and model peptides in vitro[60−62] and in phytochelatins the strength of metal binding is higher with length of the peptides (i.e., with more cysteine).[63,64] Phytochelatin−metal complexes can be stabilized if plants or fungi produce excess sulfide.[65−67] Phytochelatins, MTs, and intracellular sulfide production may all explain Hg-rich granules in roots of plants grown in vivo[68−70] and in a contaminated saltmarsh.[71]

In the Everglades peats, the S_{red} in the thiolate ligands that formed the experimental Hg_4S_x type of clusters may originate as cysteine in MTs or phytochelatins in sawgrass (2BS), cattail (F1) (SI), and periphyton[72] or in MTs produced by aquatic invertebrates,[73] fungi, and bacteria. Thiols also could have been added to the peats during bacterial reduction of aqueous sulfate.[20]

The two new Hg-SR structures we identified may elucidate other interactions between OM and Hg species. Formation of mercury-thiolate clusters might explain why metacinnabar was inhibited from precipitating in DOM solutions to which Hg was added first ($<5 \times 10^{-8}$ M; S_{red}/Hg ~ 60) followed by sulfide.[74] A thiolated aromatic structure could clarify why cinnabar dissolution rates increased with greater aromaticity of DOM and not reduced sulfur content.[75,76] Multinuclear clusters might be retained and/or nucleate HgS minerals as peat transforms to coal during burial. This is supported by isotopic signatures of presumed organic-bound vs hydrothermally sourced Hg in coal.[77]

Mercury-SR bonds, in general, could also explain the origin of Hg in petroleum or natural gas.

The observed Hg-SR structures raise other questions. What is the origin of the mercury-thiolate cluster? Are metalloproteins and peptides added to peat directly from plants and other organisms living in the aquatic environment? If so, did the Hg added during the experiments displace other trace metals originally complexed in these biomolecules? Is the Hg_4S_x cluster the strongest binding site for Hg in peat and by implication other forms of natural organic matter, and if so, is this Hg available or unavailable for methylation? Further characterization of specific biomolecules in macromolecular natural organic matter would be a step forward toward linking cellular functions in living organisms to sequestration of trace metals by organic materials in the earth.

■ ASSOCIATED CONTENT

Supporting Information. Descriptions of methods. Adsorption isotherms. Model fits of S-K edge XANES and Hg-L_3 EXAFS spectra with tables of fit parameters. Microfluorescence and microdiffraction analysis for S and Fe−S species. This material is available free of charge via the Internet at http://pubs.acs.org.

■ AUTHOR INFORMATION

Corresponding Author

*Phone: (312) 355-3276; e-mail: klnagy@uic.edu.

Present Addresses

[⊥]Integral Consulting Inc., 285 Century Place, Suite 190, Louisville, Colorado 80027.

■ ACKNOWLEDGMENT

Support was provided to K.LN. and J.N.R. from NSF grants EAR-0447310 and EAR-0447386; to K.L.N., A.M., G.R.A., and J.N.R. by the Office of Science (BER), U.S. DOE; to A.M. from the ANR-CNRS-ECCO Program; and, to G.R.A. from the U.S. Geological Survey Priority Ecosystems Science Program. We thank K. Butler (USGS), J.L. Hazemann (CNRS), O. Proux (CNRS), and M. Marcus (ALS) for their technical assistance and B. Lanson and N. Findling (CNRS, ISTerre) for the XRD analysis of cinnabar and metacinnabar (SI). Beamtime at the ESRF was provided by the French CRG program of the CNRS and by the ESRF. The ALS is supported by the Director, Office of Science, Office of Basic Energy Sciences, Materials Sciences Division of the U.S. Department of Energy under Contract DE-AC03-76SF00098 at the Lawrence Berkeley National Laboratory. The use of brand names is for identification purposes only and does not imply endorsement by the USGS. We thank three anonymous reviewers who provided thoughtful comments used in revising the manuscript.

■ REFERENCES

(1) Benoit, J. M.; Gilmour, C. C.; Mason, R. P.; Heyes, A. Sulfide controls on mercury speciation and bioavailability to methylating bacteria in sediment pore waters. *Environ. Sci. Technol.* **1999**, *33*, 951–957.

(2) Schaefer, J. K.; Morel, F. M. M. High methylation rates of mercury bound to cysteine by *Geobacter sulfurreducens*. *Nat. Geosci.* **2009**, *2*, 92–93.

(3) Pickhardt, P. C.; Fisher, N. S. Accumulation of inorganic and methylmercury by freshwater phytoplankton in two contrasting water bodies. *Environ. Sci. Technol.* **2007**, *41*, 125–131.

(4) Gorski, P. R.; Armstrong, D. E.; Hurley, J. P.; Krabbenhoft D. P. Influence of natural dissolved organic carbon on the bioavailability of mercury to a freshwater alga. *Environ. Pollut.* **2008**, *154* 116–123.

(5) Hammerschmidt, C. R.; Fitzgerald, W. F.; Balcom, P. H.; Visscher, P. T. Organic matter and sulfide inhibit methylmercury production in sediments of New York/New Jersey Harbor. *Mar. Chem.* **2008**, *109*, 165–182.

(6) Cheesman, B. V.; Arnold, A. P.; Rabenstein, D. L. Nuclear magnetic resonance studies of the solution chemistry of metal complexes. 25. Hg(thiol)3 complexes and Hg(II)-thiol ligand exchange kinetics. *J. Am. Chem. Soc.* **1988**, *110*, 6359–6364.

(7) Skyllberg, U.; Xia, K.; Bloom, P. R.; Nater, E. A.; Bleam, W. F. Binding of mercury to reduced sulfur in soil organic matter along upland-peat soil transects. *J. Environ. Qual.* **2000**, *29*, 855–865.

(8) Haitzer, M.; Aiken, G. R.; Ryan, J. N. Binding of mercury(II) to dissolved organic matter: The role of the mercury-to-DOM concentration ratio. *Environ. Sci. Technol.* **2002**, *36*, 3564–3570.

(9) Drexel, R. T.; Haitzer, M.; Ryan, J. N.; Aiken, G. R.; Nagy, K. L. Mercury(II) sorption to two Florida Everglades peats: Evidence for strong and weak binding and competition by dissolved organic matter released from the peat. *Environ. Sci. Technol.* **2002**, *36*, 4058–4064.

(10) Haitzer, M.; Aiken, G. R.; Ryan, J. N. Binding of mercury(II) to aquatic humic substances: Influence of pH and source of humic substances. *Environ. Sci. Technol.* **2003**, *37*, 2436.

(11) Hsu-Kim, H.; Sedlak, D. L. Strong Hg(II) complexation in municipal wastewater effluent and surface waters. *Environ. Sci. Technol.* **2003**, *37*, 2743–2749.

(12) Han, S.; Gill, G. A. Determination of mercury complexation in coastal and estuarine waters using competitive ligand exchange method. *Environ. Sci. Technol.* **2005**, *39*, 6607–6615.

(13) Khwaja, A. R.; Bloom, P. R.; Brezonik, P. L. Binding constants of divalent mercury (Hg^{2+}) in soil humic acids and soil organic matter. *Environ. Sci. Technol.* **2006**, *40*, 844–849.

(14) Gasper, J. D.; Aiken, G. R.; Ryan, J. N. A critical review of three methods used for the measurement of mercury (Hg^{2+})-dissolved organic matter stability constants. *Appl. Geochem.* **2007**, *22*, 1583–1597.

(15) Skyllberg, U. Competition among thiols and inorganic sulfides and polysulfides for Hg and MeHg in wetland soils and sediments under suboxic conditions: Illumination of controversies and implications for MeHg net production. *J. Geophys. Res.* **2008**, *113*, 1–14.

(16) Xia, K.; Skyllberg, U. L.; Bleam, W. F.; Bloom, P. R.; Nater, E. A.; Helmke, P. A. X-ray absorption spectroscopic evidence for the complexation of Hg(II) by reduced sulfur in soil humic substances. *Environ. Sci. Technol.* **1999**, *33*, 257–261.

(17) Hesterberg, D.; Chou, J. W.; Hutchison, K. J.; Sayers, D. E. Bonding of Hg(II) to reduced organic sulfur in humic acid as affected by S/Hg ratio. *Environ. Sci. Technol.* **2001**, *35*, 2741–2745.

(18) Skyllberg, U.; Bloom, P. R.; Qian, J.; Lin, C.-M.; Bleam, W. F. Complexation of mercury(II) in soil organic matter: EXAFS evidence for linear two-coordination with reduced sulfur groups. *Environ. Sci. Technol.* **2006**, *40*, 4174–4180.

(19) Manceau, A.; Nagy, K. L. Relationships between Hg(II)-S bond distance and Hg(II) coordination in thiolates. *Dalton Trans.* **2008**, 1421–1425.

(20) Gilmour, C. C.; Riedel, G. S.; Ederington, M. C.; Bell, J. T.; Gill, G. A.; Stordal, M. A. Methylmercury concentrations and production rates across a trophic gradient in the northern Everglades. *Biogeochemistry* **1998**, *40*, 327–345.

(21) Jew, A. D.; Kim, C. S.; Rytuba, J. J.; Gustin, M. S.; Brown, G. E., Jr. New technique for quantification of elemental Hg in mine wastes and its implications for mercury evasion into the atmosphere. *Environ. Sci. Technol.* **2011**, *45*, 412–417.

(22) Potter, R. W.; Barnes, H. L. Phase relations in the binary Hg-S. *Am. Mineral.* **1978**, *63*, 1143–1152.

(23) Kasama, T.; Church, N. S.; Feinberg, J. M.; Dunin-Borkowski, R. E.; Harrison, R. J. Direct observation of ferrimagnetic/ferroelastic

domain interactions in magnetite below the Verwey transition. *Earth Planet. Sci. Lett.* **2010**, *297*, 10–17.

(24) Manceau, A.; Matynia, A. The nature of Cu bonding to natural organic matter. *Geochim. Cosmochim. Acta* **2010**, *74*, 2556–2580.

(25) Andrews, J. C. Mercury speciation in the environment using X-ray absorption spectroscopy. *Struct. Bonding (Berlin, Ger.)* **2006**, *120*, 1–35.

(26) Freisinger, E. Plant MTs-long neglected members of the metallothionein superfamily. *Dalton Trans.* **2008**, *47*, 6649–6852.

(27) Pickering, I. J.; George, G. N.; Dameron, C. T.; Kurz, B.; Winge, D. R.; Dance, I. G. X-ray absorption spectroscopy of cuprous-thiolate clusters in proteins and model systems. *J. Am. Chem. Soc.* **1993**, *115*, 9498–9505.

(28) Brown, K. R.; Keller, G. L.; Pickering, I. J.; Harris, H. H.; George, G. N.; Winge, D. R. Structures of the cuprous-thiolate clusters of the Mac1 and Ace1 transcriptional activators. *Biochemistry* **2002**, *41*, 6469–6476.

(29) Xiao, Z.; Loughlin, F.; George, G. N.; Howlett, G. J.; Wedd, A. G. C-terminal domain of the membrane copper transporter Ctr1 from *Saccharomyces cerevisiae* binds four Cu(I) ions as a cuprous-thiolate polynuclear cluster: Sub-femtomolar Cu(I) affinity of three proteins involved in copper trafficking. *J. Am. Chem. Soc.* **2004**, *126*, 3081–3090.

(30) Voronova, A.; W., M.-K.; Meyer, T.; Rompel, A.; Krebs, B.; J., K.; Sillard, R.; Palumaa, P. Oxidative switches in functioning of mammalian copper chaperone Cox17. *Biochem. J.* **2007**, *408*, 139–148.

(31) Stasser, J. P.; Siluvai, G. S.; Barry, A. N.; Blackburn, N. J. A multinuclear copper(I) cluster forms the dimerization interface in copper-loaded human copper chaperone for superoxide dismutase. *Biochemistry* **2007**, *46*, 11845–11856.

(32) Bogumil, R.; Faller, P.; P.-A., B.; Vašák, M.; Charnock, J. M.; Garner, C. D. Structural characterization of Cu(I) and Zn(II) sites in neuronal-growth-inhibitory factor by extended X-ray absorption fine structure (EXAFS). *Eur. J. Biochem.* **1998**, *255*, 172–177.

(33) Dance, I. G.; Calabrese, J. C. The crystal and molecular structure of the hexa-($\mu_2$benzenethiolato)tetracuprate(I) dianion. *Inorg. Chim. Acta* **1976**, *19*, L41–L42.

(34) Wright, J. G.; Tsang, H.-T.; Penner-Hahn, J. E.; O'Halloran, T. V. Coordination chemistry of the Hg-MerR metalloregulatory protein: Evidence for a novel tridentate Hg-cysteine receptor site. *J. Am. Chem. Soc.* **1990**, *112*, 2434–2435.

(35) Dieckmann, G. R.; McRorie, D. K.; Tierney, D. L.; Utschig, L. M.; Singer, C. P.; O'Halloran, T. V.; Penner-Hahn, J. E.; DeGrado, W. F.; Pecoraro, V. L. *De novo* design of mercury-binding two- and three-helical bundles. *J. Am. Chem. Soc.* **1997**, *119*, 6195–6196.

(36) Jiang, D. T.; Heald, S. M.; Sham, T. K.; Stillman, M. J. Structures of the cadmium, mercury, and zinc thiolate clusters in metallothionein: XAFS study of Zn7-MT, Cd7-MT, Hg7-MT, and Hg18-MT formed from rabbit liver metallothionein 2. *J. Am. Chem. Soc.* **1994**, *116*, 11004–11013.

(37) Hasnain, S. S. Application of EXAFS to biochemical systems. *Top. Curr. Chem.* **1988**, *147*, 73–93.

(38) Wernimont, A. K.; Huffman, D. L.; Lamb, A. L.; O'Halloran, T. V.; Rosenzweig, A. C. Structural basis for copper transfer by the metallochaperone for the Menkes/Wilson disease proteins. *Nat. Struct. Biol.* **2000**, *7*, 766–771.

(39) Steele, R. A.; Opella, S. J. Structures of the reduced and mercury-bound forms of MerP, the periplasmic protein from the bacterial mercury detoxification system. *Biochemistry* **1997**, *36*, 6885–6895.

(40) Schict, O.; Freisinger, E. Spectroscopic characterization of *Cicer arietinum* metallothionein 1. *Inorg. Chim. Acta* **2009**, *362*, 714–724.

(41) Jalilehvand, F.; Leung, B. O.; Izadifard, M.; Damian, E. Mercury-(II) cysteine complexes in alkaline aqueous solution. *Inorg. Chem.* **2006**, *45*, 66–73.

(42) Mah, V.; Jalilehvand, F. Mercury(II) complex formation with glutathione in alkaline aqueous solution. *J. Biol. Inorg. Chem.* **2008**, *13*, 541–553.

(43) Alex, S.; Savoie, R.; Corbeil, M.-C.; Beauchamp, A. L. Complexation of glycylglycine by the methylmercury cation: a vibrational spectroscopy and X-ray diffraction study. *Can. J. Chem.* **1986**, *64*, 148–157.

(44) Corbeil, M.-C.; Beauchamp, A. L.; Alex, S.; Savoie, R. Interaction of the methylmercury cation with glycine and alanine: a vibrational and X-ray diffration study. *Can. J. Chem.* **1986**, *64*, 1876–1884.

(45) Alvarez-Puebla, R. A.; Valenzuela-Calahorro, C.; Garrido, J. J. Theoretical study on fulvic acid structure, conformation and aggregation: a molecular modeling approach. *Sci. Total Environ.* **2006**, *358*, 243–254.

(46) Penner-Hahn, J. E. Characterization of "spectroscopically quiet" metals in biology. *Coord. Chem. Rev.* **2005**, *249*, 161–177.

(47) Waldron, K. J.; Robinson, N. J. How do bacterial cells ensure that metalloproteins get the correct metal? *Nat. Rev. Microbiol.* **2009**, *6*, 25–35.

(48) Morris, C. A.; Nicolaus, B.; Sampson, V.; Harwood, J. L.; Kille, P. Identification and characterization of a recombinant metallothionein protein from a marine alga, *Fucus vesiculosus*. *Biochem. J.* **1999**, *338*, 553–560.

(49) Casagrande, D. J.; Gronli, K.; Sutton, N. The distribution of sulfur and organic matter in various fractions of peat: origins of sulfur in coal. *Geochim. Cosmochim. Acta* **1980**, *44*, 25–32.

(50) Francois, R. A study of sulphur enrichment in the humic fraction of marine sediments during early diagenesis. *Geochim. Cosmochim. Acta* **1987**, *51*, 17–27.

(51) Ferdelman, T. G.; Church, T. M.; Luther, G. W., III Sulfur enrichment of humic substances in a Delaware salt marsh sediment core. *Geochim. Cosmochim. Acta* **1991**, *55*, 979–988.

(52) Herkorn, N.; Benner, R.; Frommberger, M.; Schmitt-Kopplin, P.; Witt, M.; Kaiser, K.; Kettrup, A.; Hedges, J. I. Characterization of a major refractory component of marine dissolved organic matter. *Geochim. Cosmochim. Acta* **2006**, 70.

(53) Lam, B.; Baer, A.; Alaee, M.; Lefebvre, B.; Moser, A.; Williams, A.; Simpson, A. J. Major structural components in freshwater dissolved organic matter. *Environ. Sci. Technol.* **2007**, *41*, 8240–8247.

(54) Presta, A.; Fowle, D. A.; Stillman, M. J. Structural model of rabbit liver copper metallothionein. *Dalton Trans.* **1997**, 977–984.

(55) Blindauer, C. A.; Razi, M. T.; Campopiano, D. J.; Sadler, P. J. Histidine ligands in bacterial metallothionein enhance cluster stability. *J. Biol. Inorg. Chem.* **2007**, *12*, 393–405.

(56) Maret, W.; Vallee, B. L. Thiolate ligands in metallothionein confer redox activity on zinc clusters. *Proc. Natl. Acad. Sci. U. S. A.* **1998**, *95*, 3478–3482.

(57) Song, F.; Briseno, A. L.; Zhou, F. Redox reactions of and transformation between cysteine-mercury thiolate and cystine in metallothioneins adsorbed at a thin mercury film electrode. *Langmuir* **2001**, *17*, 4081–4089.

(58) Duncan, K. E. R.; Ngu, T. T.; Chan, J.; Salgado, M. T.; Merrifield, M. E.; Stillman, M. J. Peptide folding, metal-binding mechanisms, and binding site structures in metallothioneins. *Exp. Biol. Med.* **2006**, *231*, 1488–1499.

(59) Robinson, N. J.; Tommey, A. M.; Kuske, C.; Jackson, P. J. Plant metallothioneins. *Biochem. J.* **1993**, *295*, 1–10.

(60) Vašák, M., Metal removal and substitution in vertebrate and invertebrate metallothioneins. *Methods Enzymol.* Eds.; **1991**, *205*, 452−458.

(61) Stillman, M. J. Metallothioneins. *Coord. Chem. Rev.* **1995**, *144* 461–511.

(62) Rousselot-Pailley, P.; Sénèque, O.; Lebrun, C.; Crouzy, S.; Boturyn, D.; Dumy, P.; Ferrand, M.; P., D. Model peptides based on the binding loop of the copper metallochaperone Atx1: Selectivity of the consensus sequence MxCxxC for metal ions Hg(II), Cu(I), Pb(II), and Zn(II). *Inorg. Chem.* **2006**, *45*, 5510–5520.

(63) Mehra, R. K.; Miclat, J.; Kodati, V. R.; Abdullah, R.; Hunter, T. C.; Mulchandani, P. Optical spectroscopic and reverse-phase HPLC analyses of Hg(II) binding to phytochelatins. *Biochem. J.* **1996**, *314*, 73–82.

(64) Checkmeneva, E.; Diaz-Cruz, J. M.; Arino, C.; Esteban, M. Binding of Hg^{2+} with phytochelatins: Study by differential pulse voltammetry on rotating Au-disk electrode, electrospray ionization mass-spectrometry, and isothermal titration calorimetry. *Environ. Sci. Technol.* **2009**, *43*, 7010–7015.

(65) Reese, R. N.; Winge, D. R. Sulfide stabilization of the cadmium-γ-glutamyl peptide complex of *Schizosaccharomyces pombe*. *J. Biol. Chem.* **1988**, *263*, 12832–12835.

(66) Steffens, J. C. The heavy-metal binding peptides of plants. *Annu. Rev. Plant Physiol. Plant Mol. Biol.* **1990**, *41*, 553–575.

(67) Dameron, C. T.; Reese, R. N.; Mehra, R. K.; Kortan, A. R.; Carroll, P. J.; Steigerwald, M. L.; Brus, L. E.; Winge, D. R. Biosynthesis of cadmium sulphide quantum semiconductor crystallites. *Nature* **1989**, *338*, 596–597.

(68) Velasco-Alinsug, M. P.; Rivero, G. C.; Quibuyen, T. A. O. Isolation of mercury-binding peptides in vegetative parts of *Chromolaena odorata*. *Z. Naturforsch., C: J. Biosci.* **2005**, *60c*, 252–259.

(69) Iglesia-Turiño, S.; Febrero, A.; Jauregui, O.; Caldelas, C.; Araus, J. L.; J., B. Detection and quantification of unbound phytochelatin 2 in plant extracts of *Brassica napus* growth with different levels of mercury. *Plant Physiol.* **2006**, *142*, 742–749.

(70) Patty, C.; Barnett, B.; Mooney, B.; Kahn, A.; Levy, S.; Liu, Y.; Pianetta, P.; Andrews, J. C. Using X-ray microscopy and Hg L3 XANES to study Hg binding in the rhizosphere of *Spartina* cordgrass. *Environ. Sci. Technol.* **2009**, *43*, 7397–7402.

(71) Válega, M.; Lima, A. I. G.; Figueira, E. M. A. P.; Pereira, E.; Pardal, M. A.; Duarte, A. C. Mercury intracellular partitioning and chelation in a salt marsh plant, *Halimione portulacoides* (L.) Aellen: Strategies underlying tolerance in environmental exposure. *Chemosphere* **2009**, 74.

(72) Perales-Vela, H. G.; Peña-Castro, J. M.; Cañizares-Villanueva, R. O. Heavy metal detoxifiation in eukaryotic microalgae. *Chemosphere* **2006**, *64*, 1–10.

(73) Amiard, J.-C.; Amiard-Triquet, C.; Barka, S.; Pellerin, J.; Rainbow, P. S. Metallothioneins in aquatic invertebrates: Their role in metal detoxification and their use as biomarkers. *Aquat. Toxicol.* **2006**, *76*, 160–202.

(74) Ravichandran, M.; Aiken, G. R.; Ryan, J. N.; Reddy, M. M. Inhibition of precipitation and aggregation of metacinnabar (mercuric sulfide) by dissolved organic matter isolated from the Florida Everglades. *Environ. Sci. Technol.* **1999**, *33*, 1418–1423.

(75) Ravichandran, M.; Aiken, G. R.; Reddy, M. M.; Ryan, J. N. Enhanced dissolution of cinnabar (mercuric sulfide) by dissolved organic matter isolated from the Florida Everglades. *Environ. Sci. Technol.* **1998**, *32*, 3305–3311.

(76) Waples, J. S.; Nagy, K. L.; Aiken, G. R.; Ryan, J. N. Dissolution of cinnabar (HgS) in the presence of natural organic matter. *Geochim. Cosmochim. Acta* **2005**, *69*, 1575–1588.

(77) Lefticariu, L.; Blum, J. D.; Gleason, J. D. Mercury isotope evidence for multiple mercury sources in coal from the Illinois Basin. *Environ. Sci. Technol.* **2011**, *45*, 1724–1729.

Supporting Information (SI)

Authors:

Kathryn L. Nagy,*[†] Alain Manceau,[‡] Jarrod D. Gasper,[§,||] Joseph N. Ryan,[⊥] and George R. Aiken[§]

[†]Department of Earth & Environmental Sciences, MC-186, 845 West Taylor Street, University of Illinois at Chicago, Chicago, IL 60607, USA;
[‡]ISTerre-Maison des Géosciences, CNRS and Université J. Fourier, BP 53, 38041 Grenoble Cedex 9, France;
[§]United States Geological Survey, Water Resources Division, 3215 Marine Street, Boulder, CO 80303;
[⊥]Department of Civil, Environmental, and Architectural Engineering, University of Colorado at Boulder, 428 UCB, Boulder, CO 80309-0428

Title:

Metallothionein-like multinuclear clusters of mercury(II) and sulfur in peat

Number of pages : 30
Number of tables : 3
Number of figures : 4 (Figure S1a-b ; Figure S2a-f ; Figure S3a-z, Figure S4a-b)

Table of Contents

S1. Adsorption experiments

The peats were extracted from the top 10 cm of sediment in Water Conservation Areas (WCA) 2A (F1) and 2B (2BS) of the Florida Everglades, washed with deionized water, separated into a 74-105 μm fraction by wet-sieving, air-dried, and chemically analyzed.[2, 3] After washing, the peats contained 98 (F1) and 180 (2BS) ppb Hg. The porewater at Site F1 contained more sulfide, sulfate, and DOM, and less oxygen than water at Site 2BS (0.22 vs. 0.063 x 10^{-6} mol/L H_2S_{Total}; 470 vs. 69 x 10^{-6} mol/L SO_4^{2-}; 38 vs. 17 mg C/L; and, 10 vs. 100 x 10^{-6} mol/L O_2, respectively).[3] Sediment monomethylmercury concentrations were 1.4 x 10^{-9} for the F1 site and 1.3 x 10^{-8} mol/L CH_3Hg for the 2BS site.[4] Sawgrass (*Cladium jamaicensis*) is the dominant plant at the 2BS site but cattail (*Typha domingensis*) has dominated at the eutrophic F1 site since the mid 1970s as a result of nutrient addition from canal waters.[5, 6] Using peat accumulation rates measured in 1996,[7] the top 10 cm at each site would largely represent these two different plants. Periphyton is also present at both sites. F1 periphyton has been characterized as green filamentous algae with relatively high chlorophyll a and bacteriochlorophyll[8] and no calcareous material. 2BS periphyton is calcareous.[6] Both sites have diatoms.

Experiments used 100 mg of peat in 0.25 L of 0.01 M $NaNO_3$ adjusted to an initial pH of 6.0 ± 0.03 after which aqueous Hg(II) was added in the form of $Hg(NO_3)_2$ at initial concentrations of 3 x 10^{-7} to 2 x 10^{-4} mol/L. Experiments lasted 15 h, sufficient for equilibration of the bulk adsorption reaction based on results where no change in the amount of adsorbed Hg(II) occurred after 1 h.[3] The difference between initial and final aqueous Hg(II) concentrations yielded the sorbed amount (Table S1, Figure S1). The peat was separated from the solution by centrifugation and freeze-dried for EXAFS analysis.

Released amounts of dissolved organic carbon (DOC) were 20 to 50% of those expected based on previous results.[3] Between 0.6 and 1.2% of the initial peat mass dissolved (2.55 to 4.71 mg C/L) in no pattern except that the least dissolution occurred for the highest initial Hg concentrations (2BS-99 and F1-99). In 6 out of 7 cases, the 2BS peat produced slightly less DOC at a given initial Hg concentration. Final pH after reaction decreased by 0.2 to 0.7 pH units with lower values corresponding to higher Hg(II) loadings. Within the error of the pH measurement (± 0.02 pH units), the observed changes are within those expected for simple exchange of two hydroniums for every Hg^{2+} adsorbed.

Table S1. Data for adsorption experiments.

Expt.	$Hg(II)_{peat}$ mg kg^{-1}	DOC mg L^{-1}	S_{red}/Hg (mol mol^{-1})	EXAFS spectra
2BS-0001	0.9	4.12	57500	na
2BS-0004	4.2	3.74	12300	na
2BS-006	59	3.43	880	RT
2BS-03	326	4.17	160	RT
2BS-4	4170	4.71	12	RT
2BS-19	19000	3.78	2.7	RT
2BS-99	99100	2.55	0.50	RT, He-T
F1-0001	1.0	4.64	78300	na
F1-0006	5.6	4.50	14000	na
F1-007	69	3.65	1140	RT, He-T
F1-03	353	4.62	220	RT, He-T
F1-4a	4120	nd	19.0	na
F1-4b	4180	4.44	18.7	RT, He-T
F1-18	18400	4.46	4.3	RT, He-T
F1-99	99100	3.11	0.80	RT, He-T

F1 peat has 1.79 wt. % S (1.25 wt.% S_{red}); 2BS peat has 1.27 wt. % S (0.83 wt. % S_{red})(see section S2)

DOC ≡ Dissolved Organic Carbon; na ≡ not applicable; nd ≡ not determined

RT ≡ spectra measured at room temperature; He-T ≡ spectra measured at liquid helium temperature (8-16 K)

Samples F1-4a and F1-4b demonstrate experimental reproducibility.

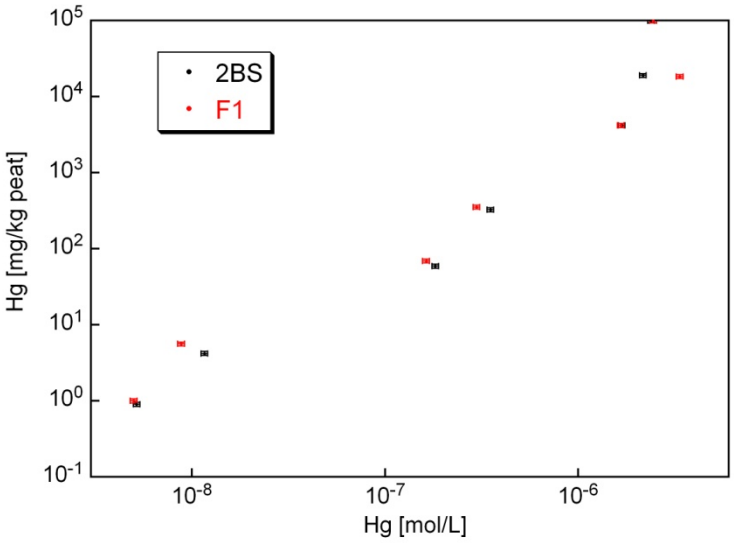

Figure S1a. Mercury(II) adsorption isotherm: Adsorbed Hg(II) vs. Solution Hg(II) at Equilibrium. Adsorbed Hg(II) per mass of 2BS (black; 6 experiments) and F1 (red; 7 experiments) peats vs. equilibrium solution concentration. Error bars represent 4% uncertainty in measured aqueous Hg concentration. Adsorbed Hg(II) was determined by difference between initial and equilibrated solution concentrations.

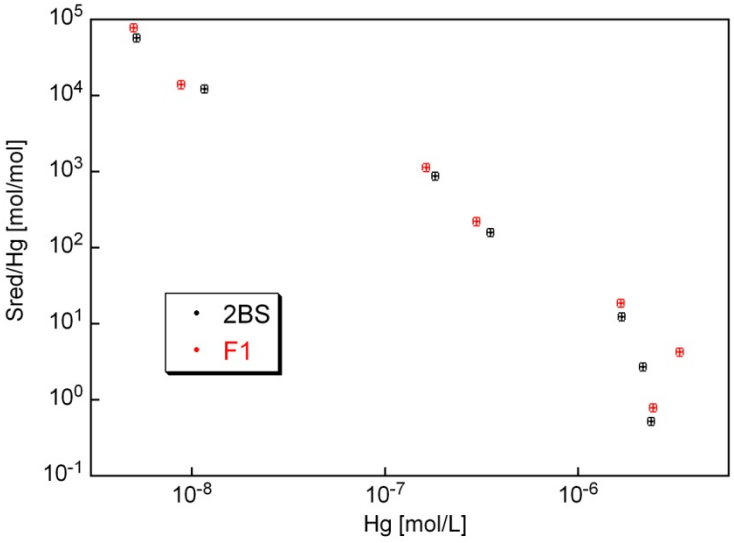

Figure S1b. Mercury(II) adsorption isotherm data recast as Reduced Sulfur/Adsorbed Hg(II) vs. Solution Hg(II) at Equilibrium: The uncertainty on the amount of reduced S is 10% (see Section 2 on XANES spectroscopy).

S2. XANES spectroscopy

S2.1. Measurements and data analysis

Sulfur K-edge XANES spectra were acquired at the Advanced Light Source (ALS, Berkeley) on the microfocus beamline 10.3.2.[9] Spectra for the 2BS and F1 peats were measured by fluorescence detection with a 7-element Ge detector and those for sulfur-containing standards in total electron yield (TEY) detection mode to prevent signal distortion by over absorption effects.[10, 11] For TEY measurements, a thin layer of fine powder was spread onto conductive graphite tape to minimize distortion to the signal induced by sample charging. Each spectrum is the average of four to ten statistically invariant scans. Energy was calibrated by setting the $CaSO_4$ peak to 2482 eV. Spectra were normalized to unity using a polynomial, then least-squares fit to known standards to determine the relative amounts (in atom % S) of S species, defined here as a type of functionality with the same 'oxidation index'.[12] Nine standards were selected, based on previous studies[13, 14-20] to best represent the major forms of S possible in NOM: dibenzyl disulfide (R-SS-R, CAS 150-60-7), DL-cystine (R-SS-R, CAS 923-32-0), dibenzyl sulfide (R-S-R, CAS 538-74-9), L-methionine (R-S-CH_3, CAS 63-68-3), L-cysteine (R-SH, CAS 52-90-4), dibenzothiophene (R-S-R, CAS 132-65-0), DL-methionine sulfoxide (R-SO-R, CAS 62697-73-8),

sodium sulfite (Na_2S, CAS 7757-83-7), cyclohexanesulfonic acid (R-SO_3-H, sulfonate), and sulfate ($CaSO_4$). Pyrite (FeS_2) was also tested as a possible component, although its concentration was expected to be below the limit of sensitivity for the fitting procedure. The fitting precision is typically within 5 % when comparing data collected under the same conditions and analyzed with the same set of reference spectra.[19] The fitting accuracy is more difficult to assess because it depends on indeterminate biases during data measurements (e.g., detector linearity), systematic errors during data reduction (e.g., background subtraction and normalization), and how well the chosen references represent the variety of sulfur functionalities. A case in point is the sulfate peak whose height is difficult to measure accurately in fluorescence mode because of over absorption effects, and in TEY mode because of the relatively limited linearity of electron detectors. Therefore, the method is not necessarily more accurate for sulfate than for sulfides, despite the factor of five difference in peak height. Overall, we agree with[11] that the accuracy of S species composition can be estimated to within 10 % of the relative amounts obtained in the fit, as long as experimental errors are carefully minimized.

An estimate of the amount of reduced S contributed by Fe-sulfide minerals was obtained using X-ray fluorescence mapping, micro-XANES spectroscopy, and micro-diffraction. Fluorescence maps were recorded at 4.033 keV with a resolution of 15×15 μm^2 and 200 ms counting time. The diffraction pattern was recorded in transmission mode at 17 keV with a Bruker 6000 CCD binned to 1024×1024 pixels.

S2.2. Results

Five components sufficed to model the F1 and 2BS data: cystine, cysteine/methionine, sulfoxide, sulfonate, and sulfate (Figure S2a,b; Table S2). The data were fit equally well with the amino acids cysteine or methionine because their spectra cannot be distinguished in a mixture. Cysteine is produced by all organisms and is common in metallothionein (MT) proteins, whereas methionine is made only by plants and is rarer in proportion in MT. Cystine, the dimer formed by a disulfide bridge between two cysteines, stabilizes the tertiary structure of proteins. A 6-component fit to F1 added 7% dibenzyl sulfide and subtracted 6% of the cysteine and 1% of the cystine, but did not change the total amount of reduced sulfur (Table S2; Figure S2c). This fit was rejected because (1) the fit quality was improved insignificantly; (2) adding dibenzyl sulfide did not also improve the fit to the 2BS peat, which was sampled from a nearby location and expected to be similar to the F1 peat; and, (3) dibenzyl sulfide, which has a reduced sulfur peak only slightly narrower than those of cysteine and methionine and is therefore indistinguishable in a mixture, has a 'non-thiolate'-like highly symmetrical sulfur binding environment, which is unlikely to occur in this proportion in OM. None of the fits supported the presence of pyrite.

The sum of methionine, cysteine, and cystine in whole *Cladium jamaicensis* (sawgrass) from a site in WCA-1 of the Florida Everglades was about 0.7 mg g^{-1}, whereas the decayed surface litter and upper 5 cm of peat formed from sawgrass contained about 1.7 mg g^{-1},[21, 22] of which approximately 0.5 mg g^{-1} was cysteine. In comparison, the amounts of cysteine in the F1 and 2BS peats as determined by S-XANES were 28 and 16 mg g^{-1}, respectively. The amount of cysteine in the plant litter and upper few cm of sawgrass peat is equivalent to 2.3 to 2.5 mol S_{red} per mol of Hg adsorbed in the F1-03 and 2BS-03 peat samples, respectively, enough to form multinuclear clusters of composition Hg_4S_x with x = 8 to 10.

The majority of the S in the peats is organic and micro-X-ray fluorescence maps of S distribution corroborate the relative difference in amounts as determined by bulk chemical analysis[3] (Figure S2d). A small amount of the S_{red} in the peats is associated with Fe (Figure S2d), and at least some of this S_{red} is pyrite based on micro-diffraction of one bright spot of S and Fe in the 2BS peat (Figure S2e). The S_{red} peak in the micro-XANES spectrum of this spot is clearly distinct from those of bulk 2BS and F1 peat (Figure S2f), yet the S is still dominantly organic. This peak was fit with 16% pyrite, 20% cystine, and 29%

cysteine. The fractions of S associated with Fe to total S in the XRF images are 6% for 2BS and 8% for F1 as obtained by summing the Kα(S) fluorescence counts from pixels containing both S and Fe and normalizing to the total S fluorescence counts. Assuming all of the Fe-S associations contain the same proportion of pyrite, the percentage of total S speciated as pyrite in the two peats are estimated as 1% in 2BS and 1.3% in F1.

Table S2. Fraction of S in species from the linear decomposition of S-XANES spectra

	Cystine	Sulfide	Cysteine	Sulfoxide	Sulfonate	Sulfate	Sum	*NSS* (10^{-3})
F1								
5-component	0.29	-	0.41	0.11	0.16	0.06	1.02	3.29
6-component	0.28	0.07	0.35	0.11	0.16	0.06	1.03	3.20
2BS								
5-component	0.31	-	0.34	0.09	0.23	0.07	1.04	3.27

NSS is the normalized sum-squares fit residual defined as $\text{sum}[(y_{exp}-y_{fit})^2]/\text{sum}[y_{exp}^2]$.

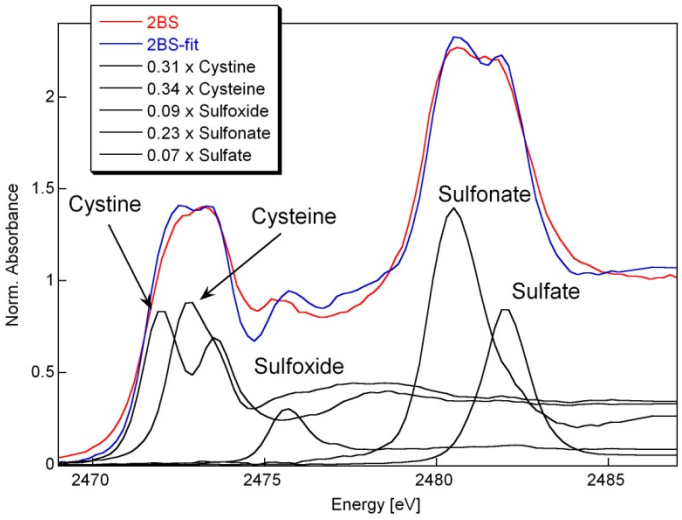

Figure S2a. Best five-component fit to S-XANES data for 2BS peat. Best fit (blue) of four reference organic sulfur compounds and one inorganic sulfate to the 2BS S-XANES data (red). 65% of the total sulfur species is reduced sulfur and can be represented by approximately equal amounts of sulfur from cysteine and cystine.

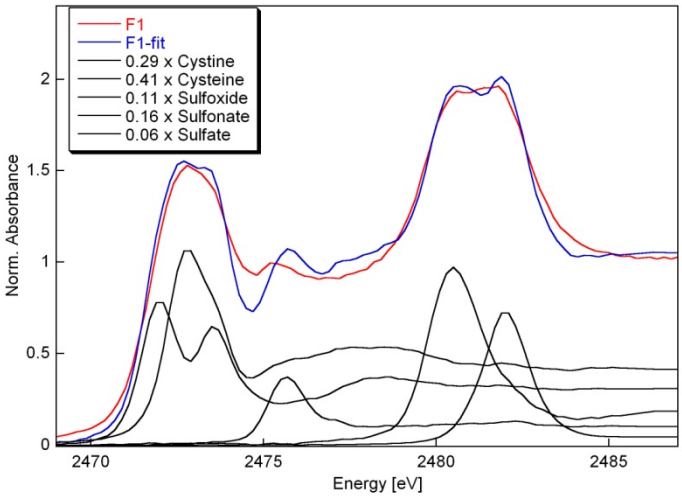

Figure S2b. Best five-component fit to S-XANES data for F1 peat. Best fit (blue) of four reference organic sulfur compounds and one inorganic sulfate to the F1 S-XANES data (red). 70% of the total sulfur species is reduced sulfur and can be represented by 41% sulfur in cysteine and 29% sulfur in cystine.

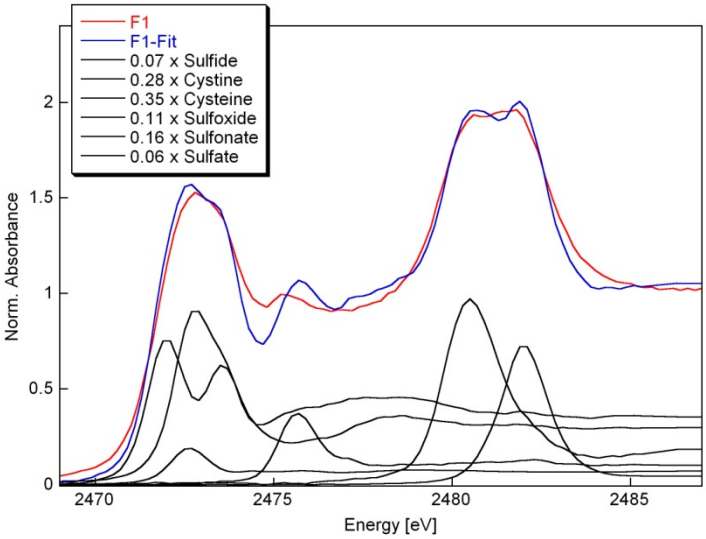

Figure S2c. Six-component fit to S-XANES spectrum of F1 peat. The fit (blue) to the spectrum (red) includes an additional component - dibenzyl sulfide. The improvement in the quality of fit over the five-component model is 9×10^{-5}, which is insignificant.

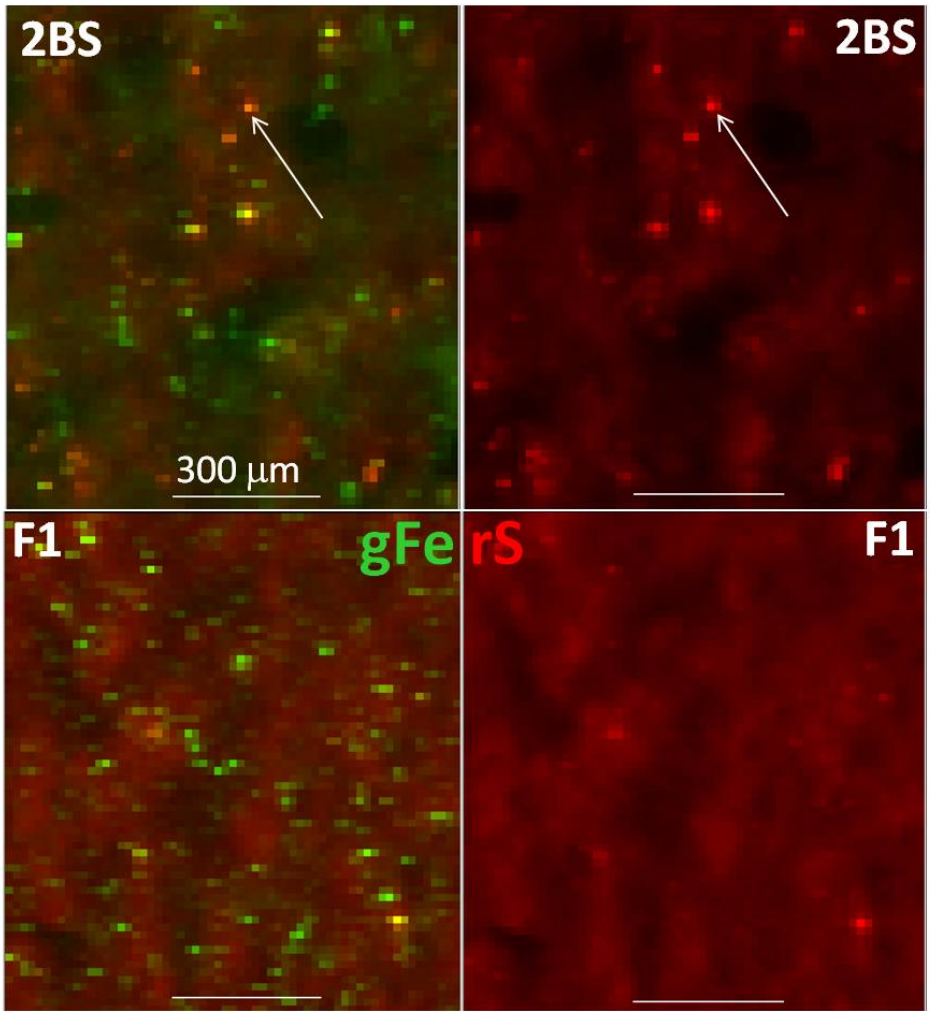

Figure S2d. Micro-X-ray fluorescence maps for the 2BS and F1 peats. Fe + S maps (left) vs. S maps (right). Arrows point to spot containing high Fe + S in 2BS analyzed with micro-X-ray diffraction (see Figure S2e) and micro-S-XANES (see Figure S2f). S is represented by red and Fe by green. Maps show qualitatively that there is more S in F1 (bottom right) than 2BS (upper right). Bright green spots on left in both samples represent unidentified Fe-oxide or Fe-oxyhydroxide phases. Orange and yellow spots in images on left indicate concentrations of Fe-S species, likely the minerals pyrite or iron-monosulfide.

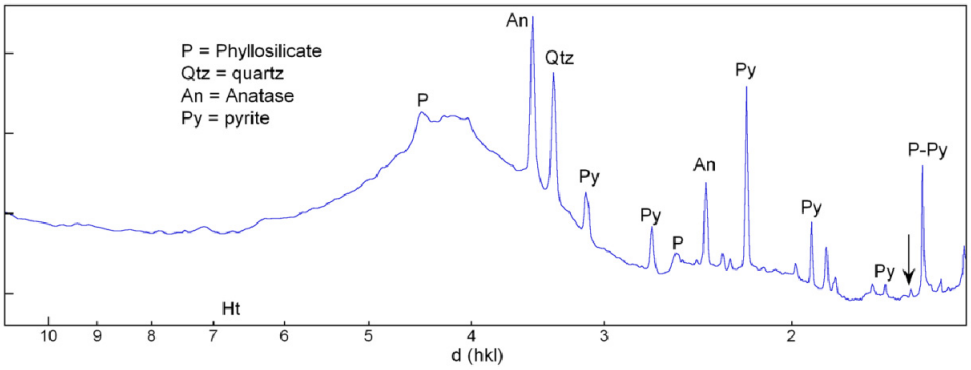

Figure S2e. Micro-X-ray diffraction of spot marked by arrow in Figure S2d. Prominent peaks of the mineral pyrite (FeS_2) and other minerals are marked.

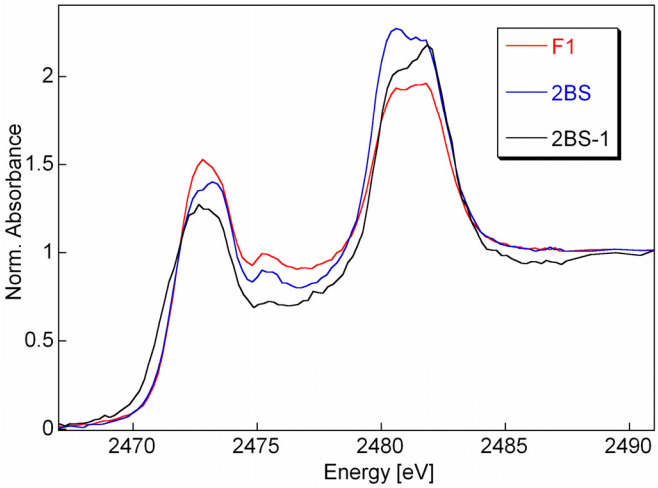

Figure S2f. Comparison of S-XANES spectra for bulk F1 and 2BS peats and spot 2BS-1. Bulk spectra were obtained by averaging five micro-XANES spectra recorded in organic rich areas. All spectra in each set were statistically invariant. The 2BS-1 spot is that marked by arrows on micro-X-ray fluorescence maps shown in Figure S2d. The reduced sulfur peak for spot 2BS-1 has a shoulder at ~2472 eV supporting the presence of FeS_2 identified by micro-XRD. However the peak shape is mostly similar to the reduced S peaks of the bulk peats which are fit entirely by a combination of the S-XANES signals for the cysteine and cystine reference materials.

S3. EXAFS spectroscopy

S3.1. Measurements and data analysis

Mercury L_3-edge X-ray absorption spectra were measured at room (RT) and 8-16 K (He-T) with a liquid helium cryostat on the FAME spectrometer (French Absorption spectroscopy beamline in Material and Environmental science - beamline BM30B[23]) at the European Synchrotron Radiation Facility (ESRF, Grenoble). Measurements were performed on 5 mm diameter pressed pellets in fluorescence-yield detection mode with a 30-element Ge detector.

The two solid references cinnabar (α-HgS; ABCR GmbH & Co KG) and metacinnabar (β-HgS, Strem Chemicals) were diluted in boron nitride to minimize over absorption,[10] and the aqueous Hg-(cysteine)$_2$ complex (2 x 10^{-3} mol/L) was prepared in a 20-25% glycerol solution. The solution reference was initially flash-frozen in liquid nitrogen. Peat samples were diluted as needed in glucose. Integration times varied from 3 s in the edge region to 15 s at k = 14 Å^{-1} for a total scan time of ca. 45 min. Multiple scans varying from 4 sweeps for concentrated to 8-10 sweeps for diluted samples were performed to optimize signal-to-noise (S/N) ratios, and the pellets were moved by 500 μm after each scan to access fresh material and improve statistics. Caution was taken that all individual spectra were statistically identical before summing them. The EXAFS oscillations were extracted, Fourier transformed, and least-squares fitted using the WinXAS 3.2 program.[24] The photon energy (E) was converted into k space using a threshold energy (E_0) set to the middle of the absorption jump. The EXAFS signal was weighted by k^3 to

compensate for the decreased amplitude at high *k*; the $k^3\chi(k)$ vs. *k* spectrum was Fourier transformed to real space with a Bessel apodization function; and structural parameters of the various coordination shells around Hg were determined by fitting data over the distance range ($R + \delta$) of interest. Theoretical amplitude and phase functions were calculated *ab initio* with FEFF v. 7,[25] using $Hg(SCH_3)_2$[26] as the structure model for the Hg-S pair and S-Hg-S multiple scattering, metacinnabar (β-HgS[27]) for the Hg-S and Hg-Hg pairs, and mercury di-acetate ($Hg(CH_3COO)_2$[28]) for the Hg-O and Hg-C pairs. The phase functions were used in the model-fits to correct the $R + \delta$ bond distances, as obtained from the Fourier transformation, for the phase-shift term (δ), which depends on the nature of the atomic pair (e.g., Hg-S, Hg-O, Hg-Hg,…). For this reason, the $R + \delta$ values reported on the *x*-axis of the Fourier transforms are apparent crystallographic *R* values. The uncertainty in the fitted distances, coordination numbers, and Debye–Waller factors were estimated at the 95 % confidence level by varying successively each fit parameter by a certain percentage and restarting the refinement with this parameter fixed.

S3.2. Results

The metacinnabar (β-HgS) reference contained 16% cinnabar based on Rietveld analysis [29] of its powder X-ray diffraction pattern (Figure S3a). The cinnabar (α-HgS) reference was pure. Therefore, we removed 16% of the RT EXAFS spectrum of cinnabar from the RT EXAFS spectrum of metacinnabar, and 16% of the He-T EXAFS spectrum of cinnabar from the He-T EXAFS spectrum of metacinnabar.

Simulations to the spectral data and corresponding Fourier transforms are provided in Figures S3b to S3z in the order: cinnabar (α-HgS), metacinnabar (β-HgS), F1-03 (S_{red}/Hg = 220), F1-4 (S_{red}/Hg = 18.7), $Hg(Cys)_2$ reference, 2BS-99 (S_{red}/Hg = 0.50), and F1-99 (S_{red}/Hg = 0.80). A theoretical simulation of the effect of temperature on the amplitude of the EXAFS signal for F1-03 is included in Figure S3l immediately following the data and simulations for F1-03. All data are presented in red in both *k*-space and *R*-space. Simulated spectra are in purple and simulated Fourier transforms are in blue. Only the modulus of each actual and modeled Fourier transform is shown for simplicity. When the actual and modeled EXAFS spectra (*k*-space) are in-phase, then the imaginary parts of their Fourier transforms (*R*-space) are in-phase as well. The nearest neighboring atoms to target element Hg are denoted above the peaks indicating their apparent bond distances (uncorrected for phase shift) in the Fourier transforms. All fit parameters, including the bond distances corrected for phase shift, are listed in Table S3. Plots in *k*-space are labeled $k^3\chi$ on the ordinate and *k* [$Å^{-1}$] on the abscissa. Plots in *R*-space are labeled FT($k^3\chi$) on the ordinate and R+δ [Å] on the abscissa. When several fit strategies were attempted, the best simulation is Model 1, unless otherwise noted. Shortcomings of other models are described below each figure.

F1-18 (S_{red}/Hg = 4.3) was not modeled *ab initio* because it is clearly a mixture of three different structural environments as determined by linear combination fitting (Figure S3x). F1-03 is not a linear combination of F1-4 (the $Hg(SR)_2$ linear structure) and cinnabar as shown by comparison of the spectra at RT (Figure S3y).

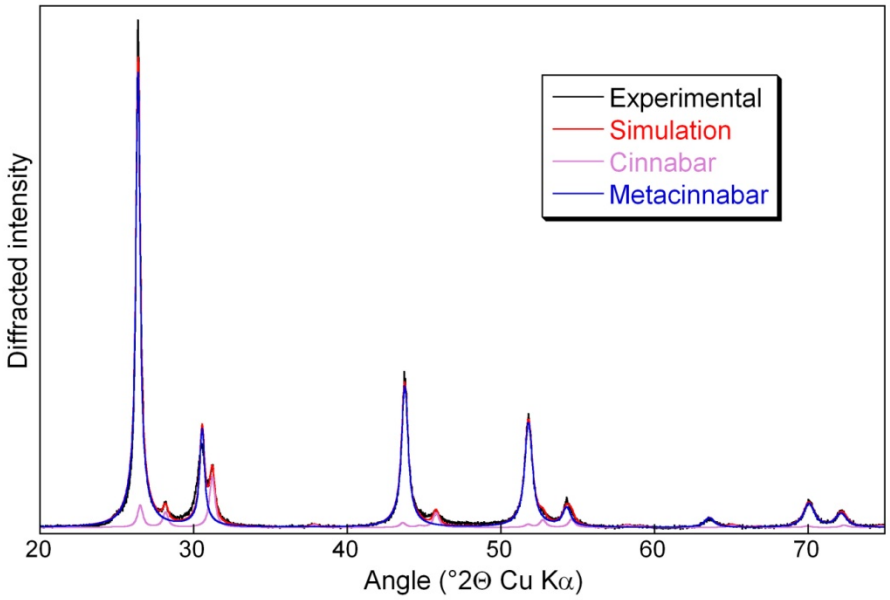

Figure S3a. Powder X-ray diffraction pattern of metacinnabar (Strem Chemicals). The amount-of-substance (i.e., mole) fraction of cinnabar = 16 % as determined by Rietveld analysis.[29]

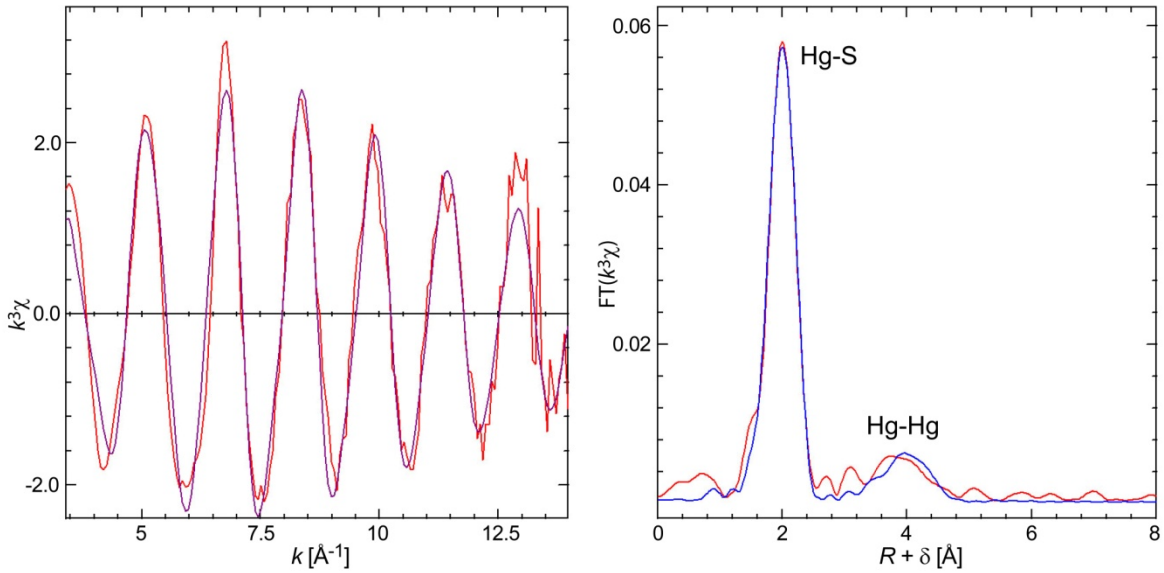

Figure S3b. **Cinnabar (α-HgS) RT - Model 1.** At RT, the Hg-S distance is dominant in the Fourier transform (right) and the Hg-Hg distance is weak in comparison. Data are in red; the modeled spectrum in *k*-space in purple (above left); and the modeled Fourier Transform (*R*-space) of the spectrum in blue (above right).

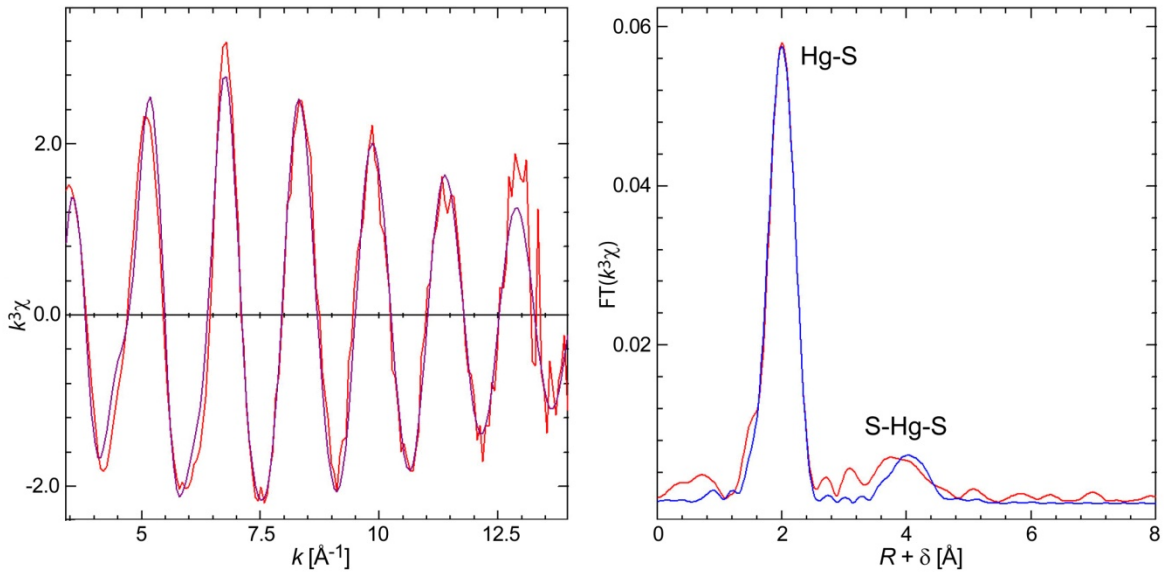

Figure S3c. **Cinnabar (α-HgS) RT - Model 2.** In comparison to Model 1, the second peak is modeled as multiple scattering from the S-Hg-S linear bonds. The two models are indistinguishable, and both multiple scattering (MS) and Hg-Hg pairs likely contribute to the peak at $R + \delta \approx 4$ Å.

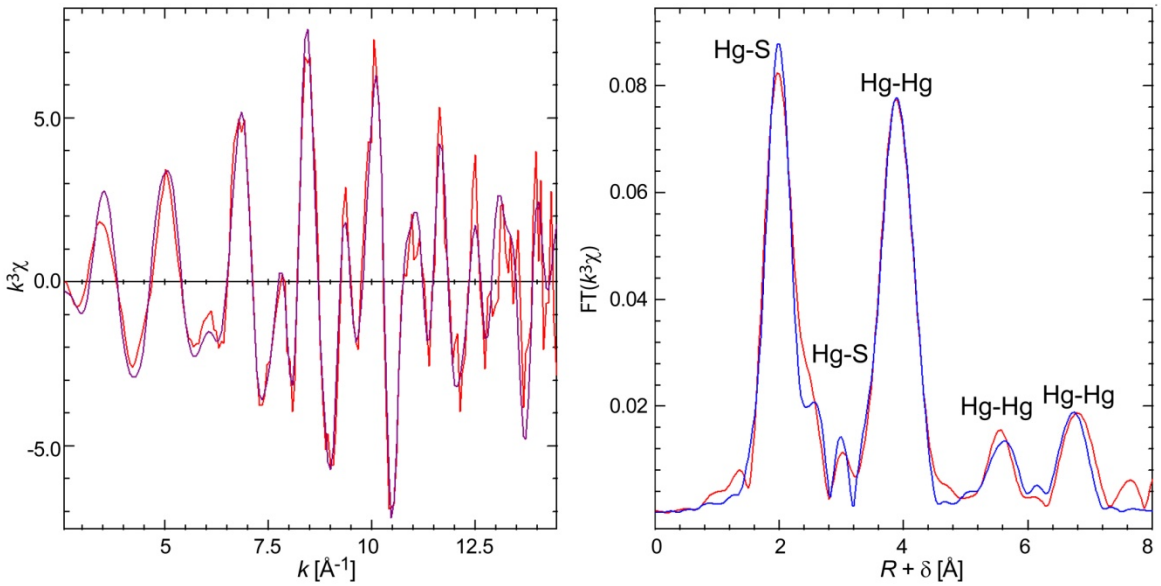

Figure S3d. **Cinnabar (α-HgS) He-T.** The two long-distance Hg-Hg pairs are at 5.67 Å and 6.82 Å. The peak at k = 6.1 Å^{-1} was reproduced by adding to the fit the four-legged MS path from the collinear S-Hg-S coordination.

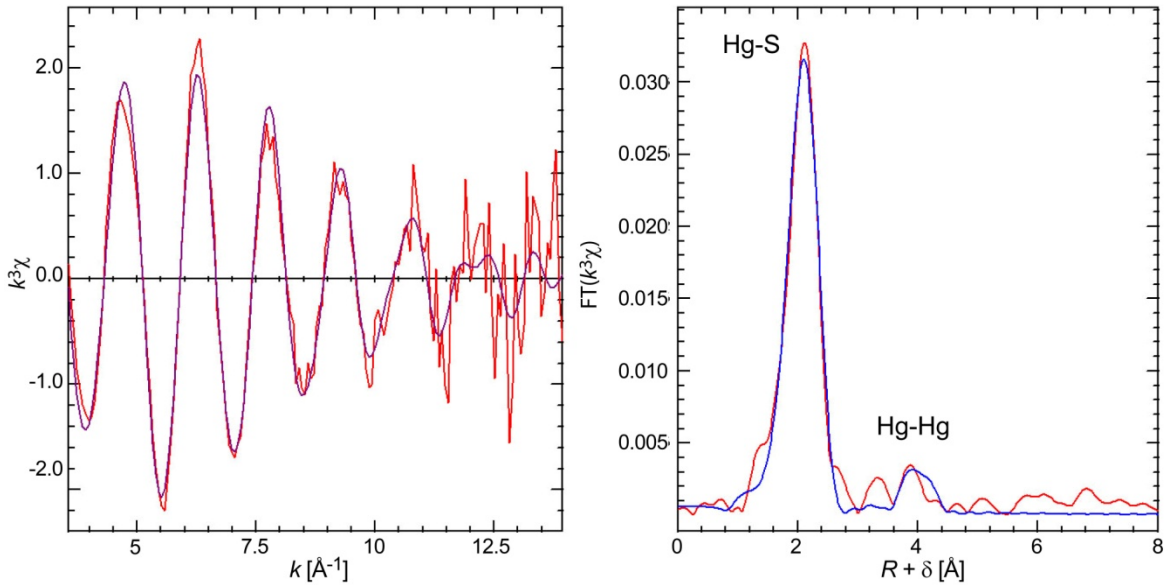

Figure S3e. **Metacinnabar (β-HgS) RT.** The measured spectrum was adjusted by removing the contribution from cinnabar which equaled 16 % as shown in Figure S3a.

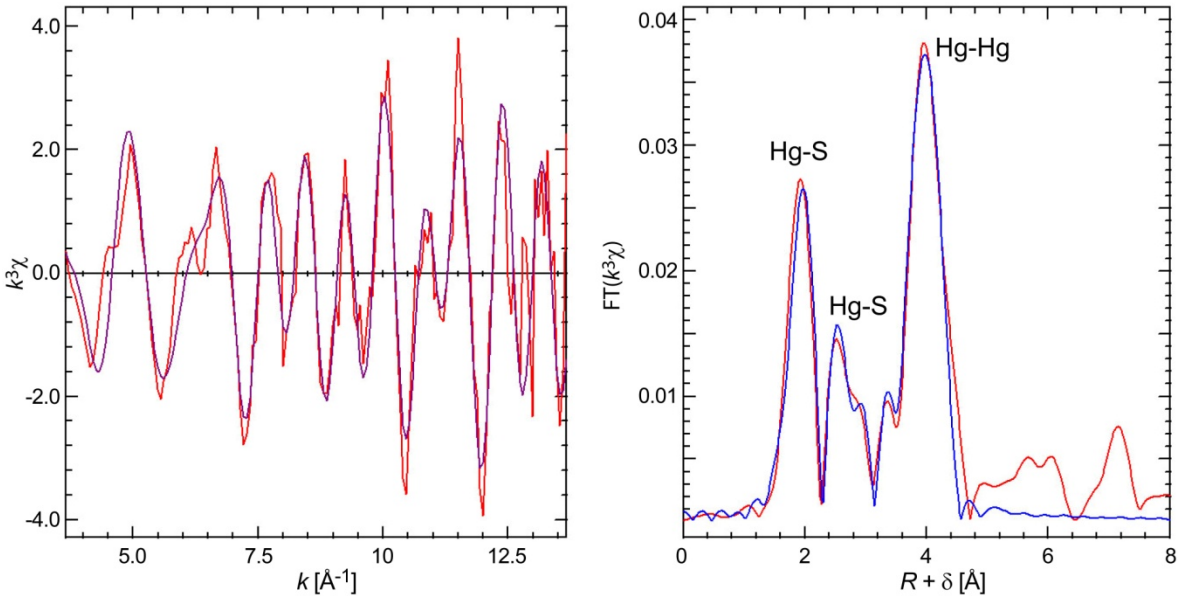

Figure S3f. **Metacinnabar (β-HgS) He-T.** The measured spectrum was adjusted by removing the contribution from cinnabar which equaled 16 % as shown in Figure S3a. The resulting spectrum and Fourier transform are similar to those of cinnabar at He-T. The misfit at k =6.1 Å^{-1} comes from the omission of the S-Hg-S MS path in the simulation (see Figure S3d).

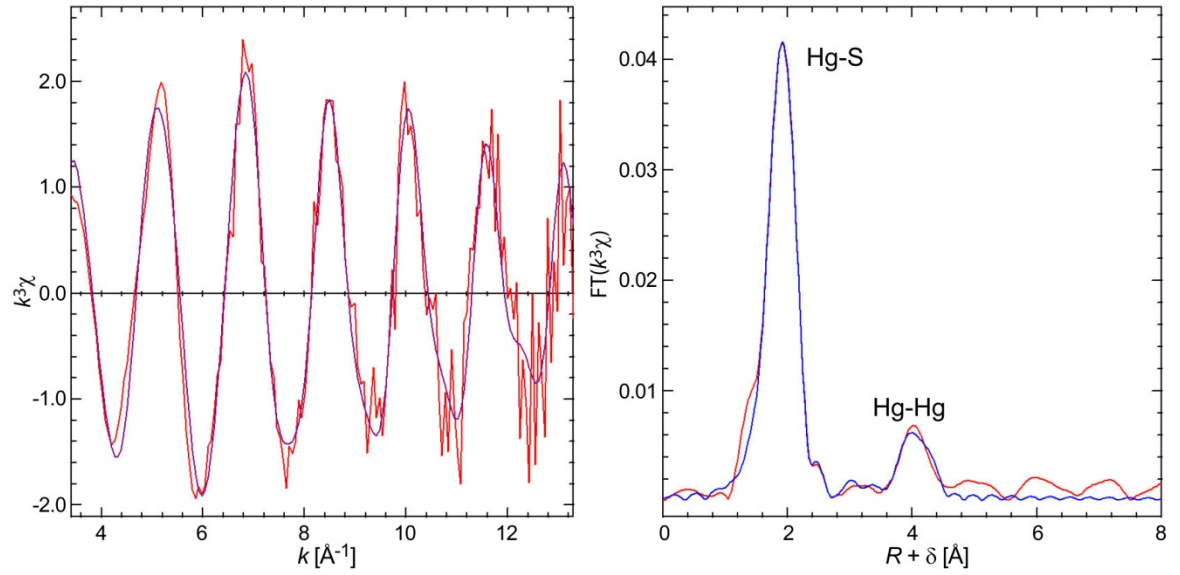

Figure S3g. **F1-03 - RT - Model 1.** The Hg-Hg pairs from the Hg_4S_x clusters are detected at room temperature, and the longer Hg-S2 distance is required to fit the main peak, labeled Hg-S. Statistical analysis with the F-test[30, 31] showed that the long Hg-S distance at 2.53 to 2.57 Å contributes to the right tail of the first peak.

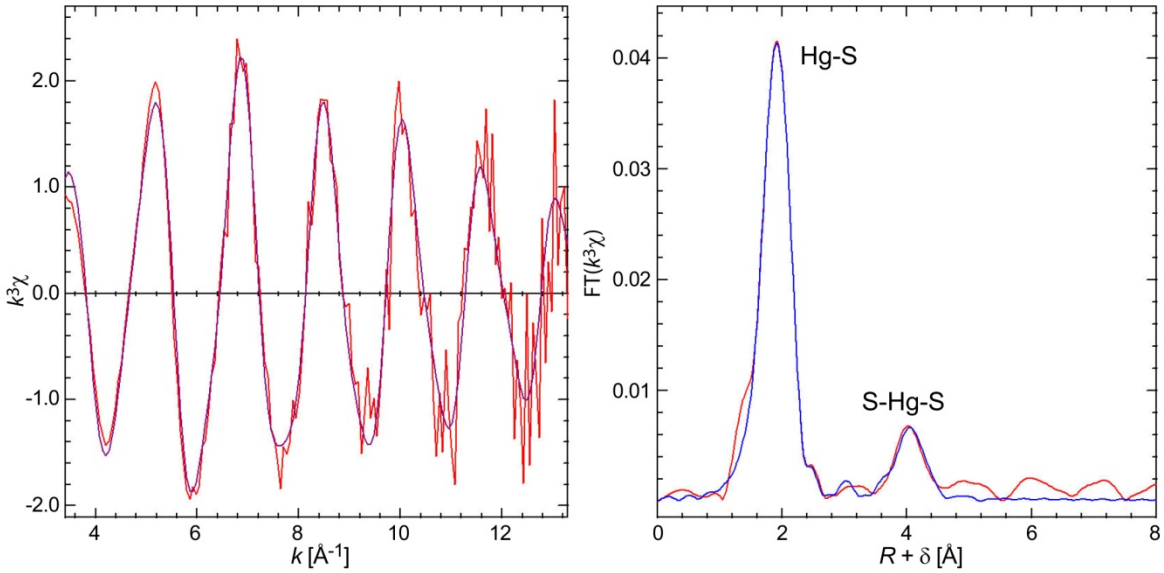

Figure S3h. **F1-03 - RT - Model 2.** When the peak at $R + \delta = 4$ Å is fit with MS paths and *CN*(MS) is allowed to float during the fit, the σ^2 value is negative.

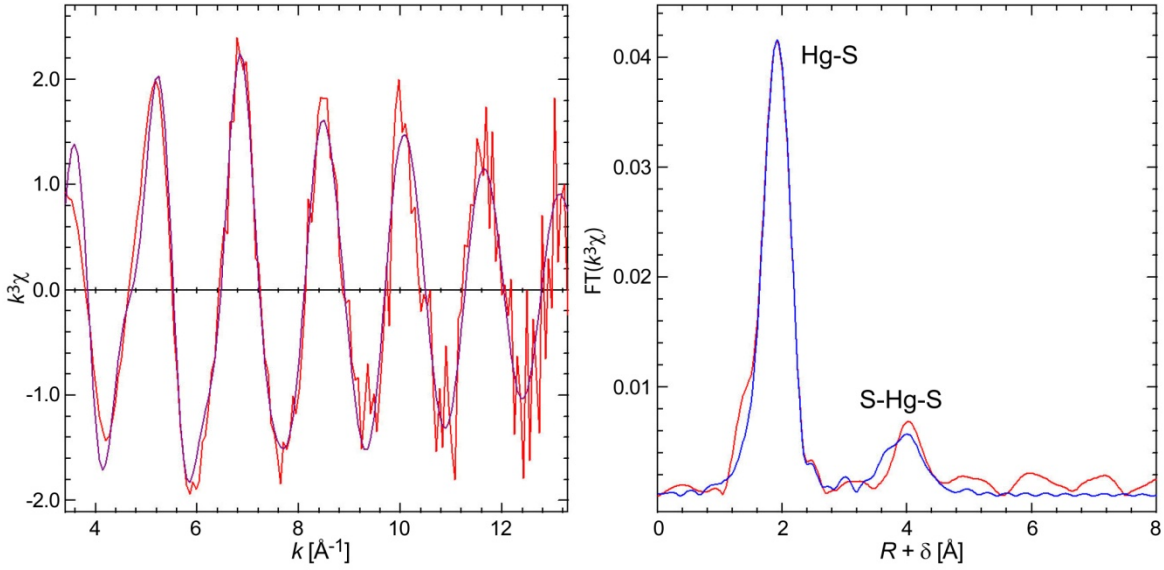

Figure S3i. **F1-03 - RT - Model 3.** When the peak at $R + \delta = 4$ Å is fit with MS paths and *CN*(MS) = *CN*(Hg-S1), as required for a collinear geometry, the quality of fit is less good by a factor of almost two compared to Model 1.

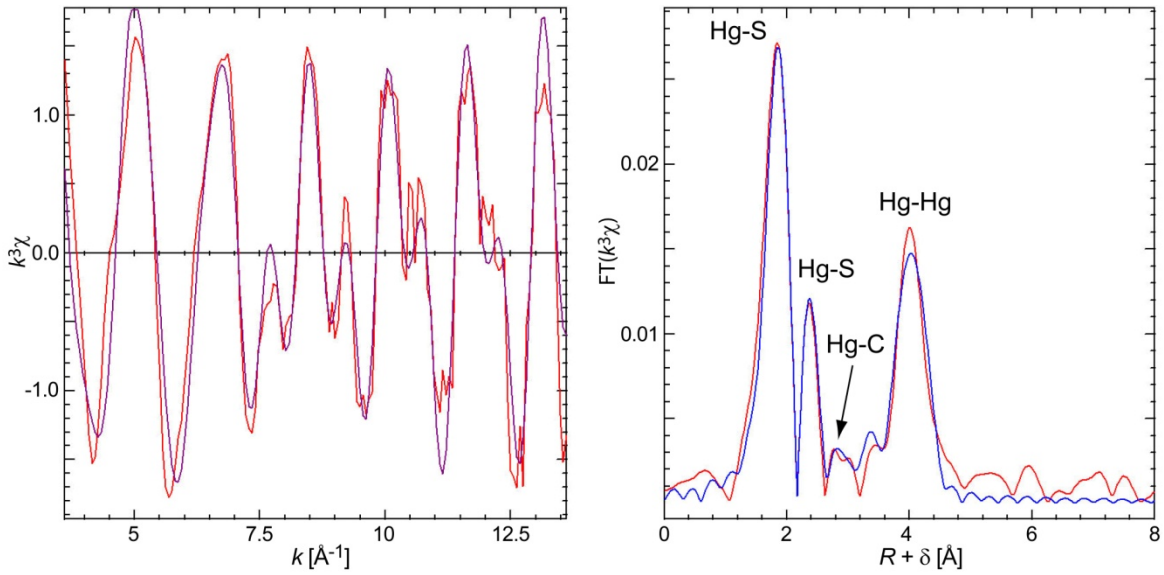

Figure S3j. **F1-03 - He-T - Model 1.**

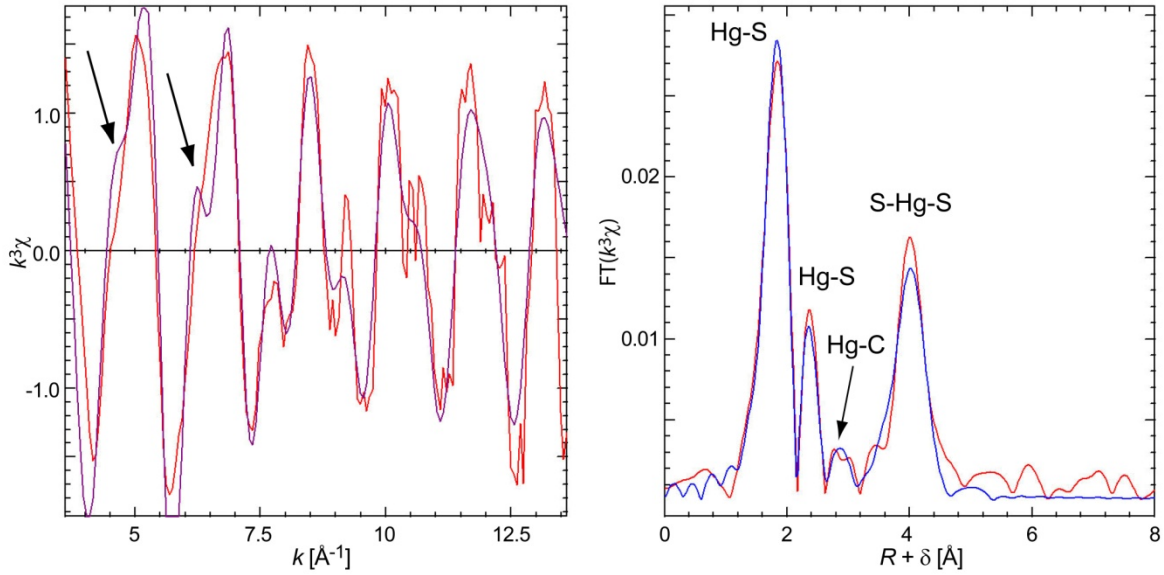

Figure S3k. **F1-03 - He-T - Model 2**. When the Fourier transform peak at $R + \delta = 4$ Å is fit with MS paths between collinear S-Hg-S atoms, as in the T-shape[32] three-coordinate model proposed previously[33], the fit quality is degraded by 50 % (Table SI-3) and the data are poorly reproduced in the 4-7 Å^{-1} k interval (first two oscillations). Also, the σ^2(S $\Leftrightarrow$ Hg $\Leftrightarrow$ S) = 0.002 Å^2 value is unrealistically low because this S-Hg-S MS path should have higher effective disorder (higher value of σ) than the Hg-S single-scattering (SS) path (σ^2(Hg-S) = 0.005 Å^2 in the model of ref 31) (e.g., as in ref 32 and 33[34, 35]).

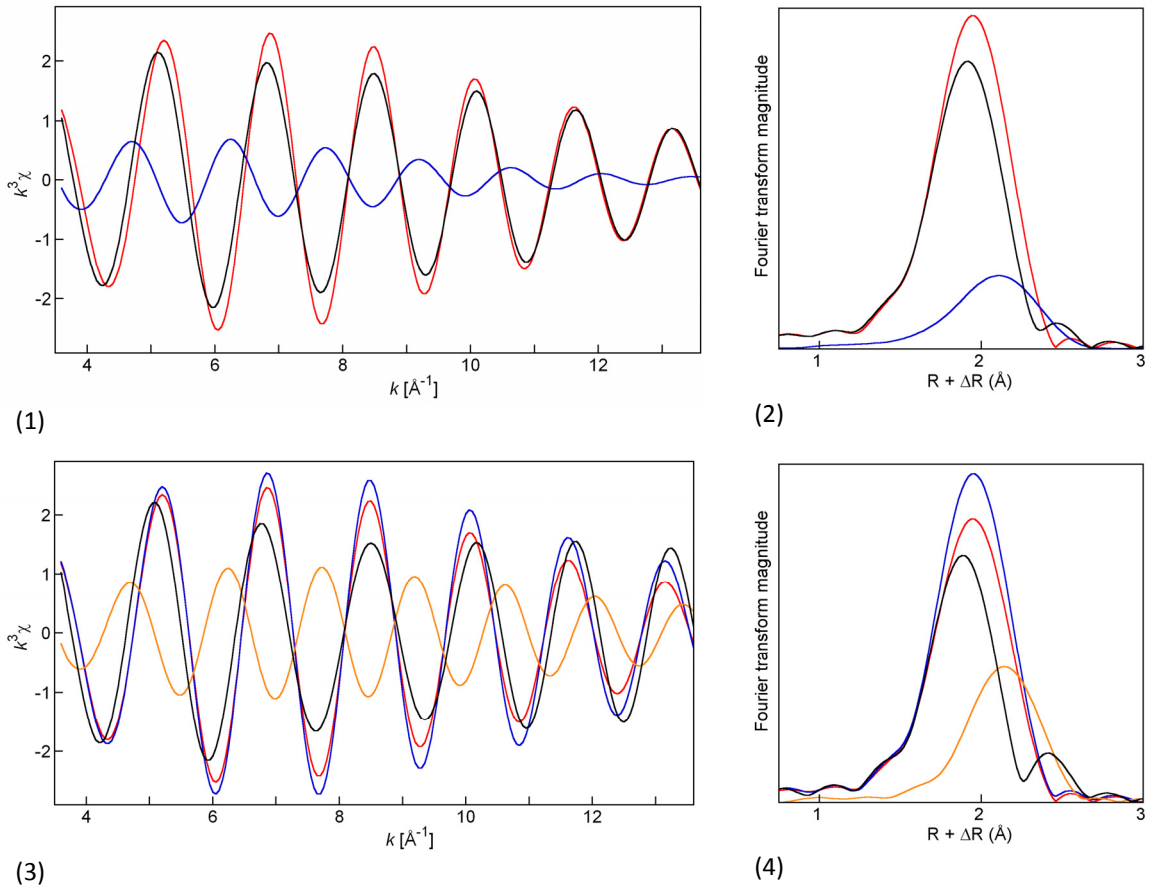

Figure S3l. **Why the amplitude of the EXAFS signal for F1-03 decreases with temperature.** The top two figures show the effect of anisotropy of the thermal motions of short and long Hg-S bonds on RT data. Theoretical EXAFS interference functions (1) and Fourier transforms (2) were calculated for the hypothetical atomic pairs:

Red: two S atoms at 2.34 Å and σ = 0.005 Å^2

Blue: one S atom at 2.53 Å and σ = 0.01 Å^2.

Black: sum

The long bond affects the phase only at low *k*, because the d(Hg-S)=2.53 Å wave is damped (i.e., is attenuated at high *k*) as a consequence of the softer character of this longer bond. In real space, the long bond gives a weak shoulder at about R + ΔR ~ 2.5 Å which can be easily mistaken for a side lobe of the Fourier transform.

The bottom two figures show the effect at He-T. Theoretical EXAFS interference functions (3) and Fourier transforms (4) were calculated for the hypothetical atomic pairs :

Red : two S atoms at 2.34 Å and σ = 0.005 Å^2.

Blue : two S atoms at 2.34 Å, but σ = 0.004 Å^2. Diminishing the Debye-Waller factor mimics the effect of lowering the temperature. The amplitudes of the EXAFS signal and FT peak increase when the disorder term (i.e., thermal agitation) decreases.

Orange : one S atom at 2.53 Å and σ = 0.004 Å^2. The wave frequency is shifted to the left at low *k*, to the right at high *k*, and is out-of-phase in the *k* region where the amplitude of the signal from the short-distance pair is maximum, i.e., at *k* = 7-9 Å^{-1}.

Black : Sum of the orange and blue curves. The composite signal from the 2S + 1S pairs is weaker than the single shell signal from the 2S pair. This counter-intuitive effect of a reduction of the EXAFS signal at low temperature is observed when two shells are amplified differently at low temperature. The longer Hg-S bond has a higher thermal motion (i.e., is 'softer'), therefore is barely detected at room temperature but appears clearly at He-T.

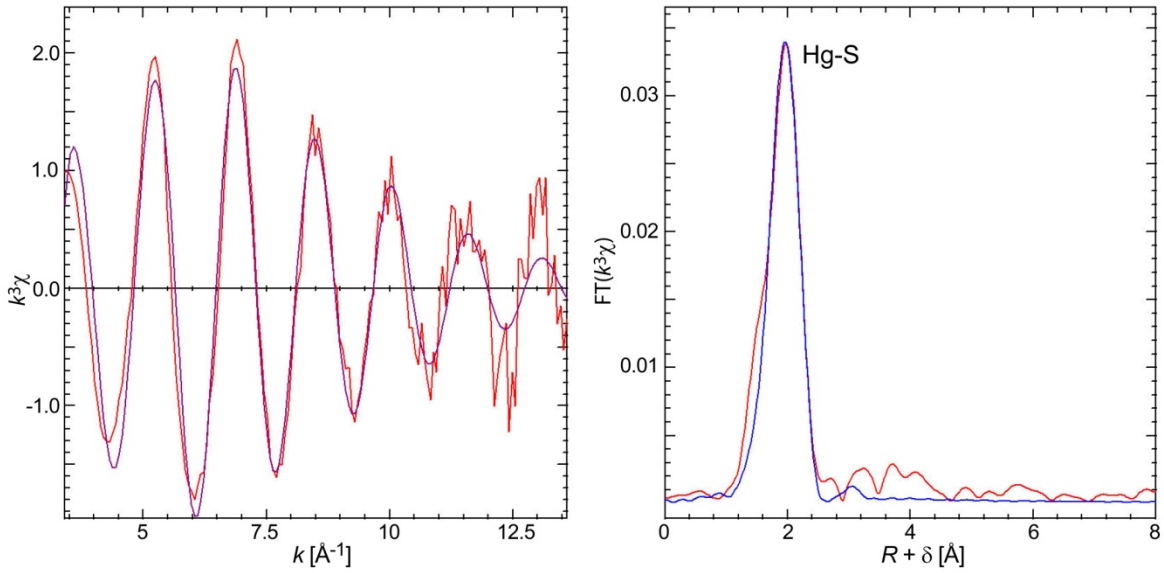

Figure S3m. **F1-4 - RT.**

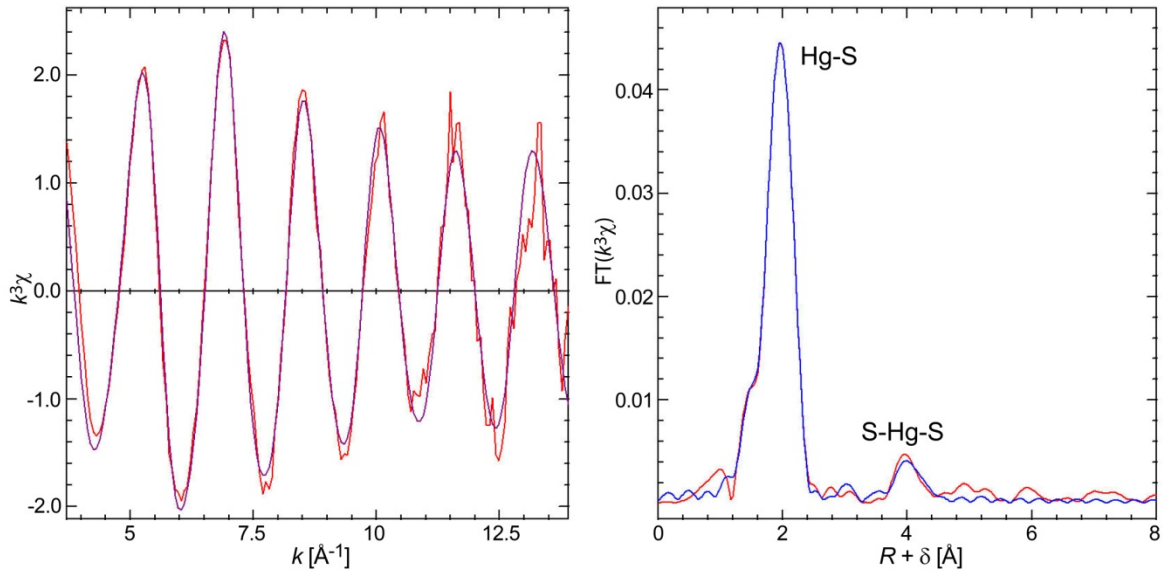

Figure S3n. **F1-4 - He-T.** The modeled distance is 4.61 Å, i.e., twice the distance for single scattering between Hg and S, and the MS scattering paths consequently have a higher Debye-Waller factor than the single-scattering paths[36] (σ^2 = 9 x 10^{-3} vs. 4 x 10^{-3} Å^2; Table S3).

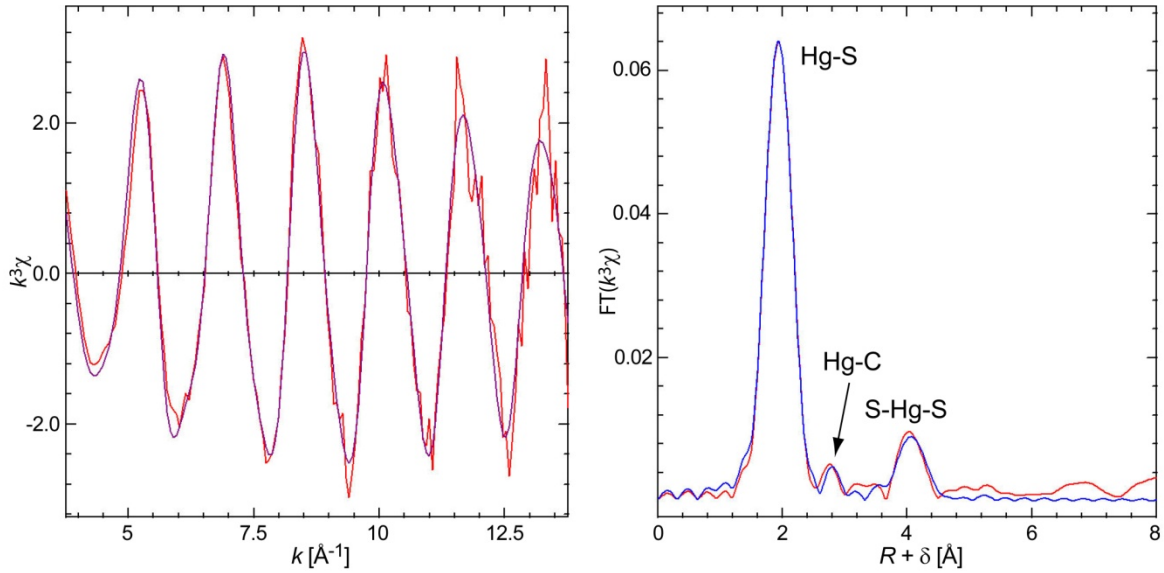

Figure S3o. **$Hg(Cys)_2$ He-T.**

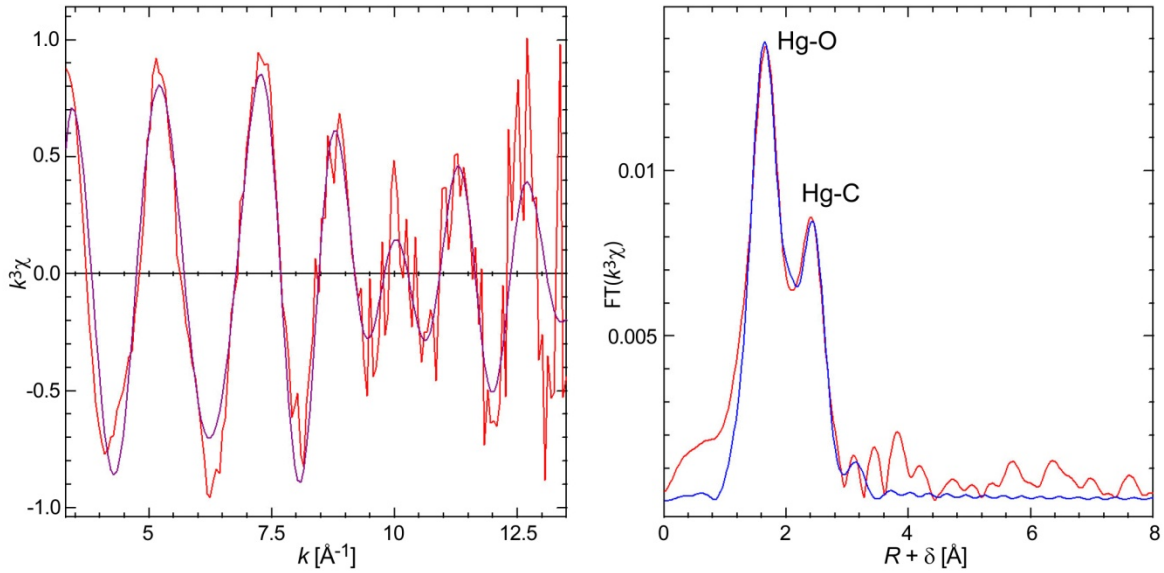

Fig. S3p. **2BS-99 - RT - Model 1.**

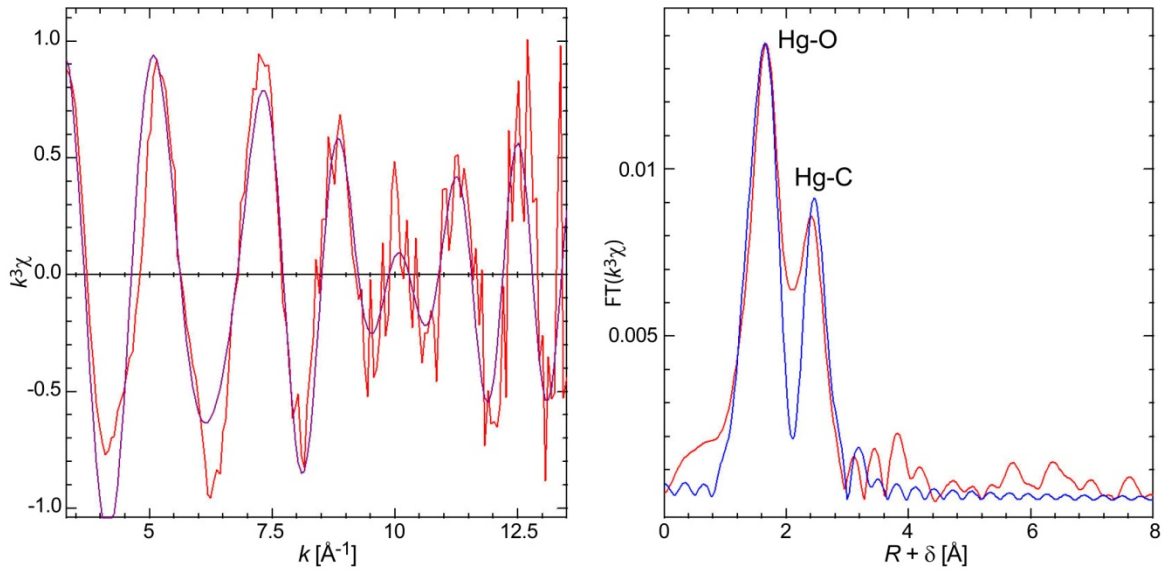

Figure S3q. **2BS-99 - RT - Model 2.** The five-membered chelate ring (with two O shells) is also detected at room temperature. The data cannot be satisfactorily reproduced with a single O shell. However, the distant C shell at about 3.3 Å is undetected.

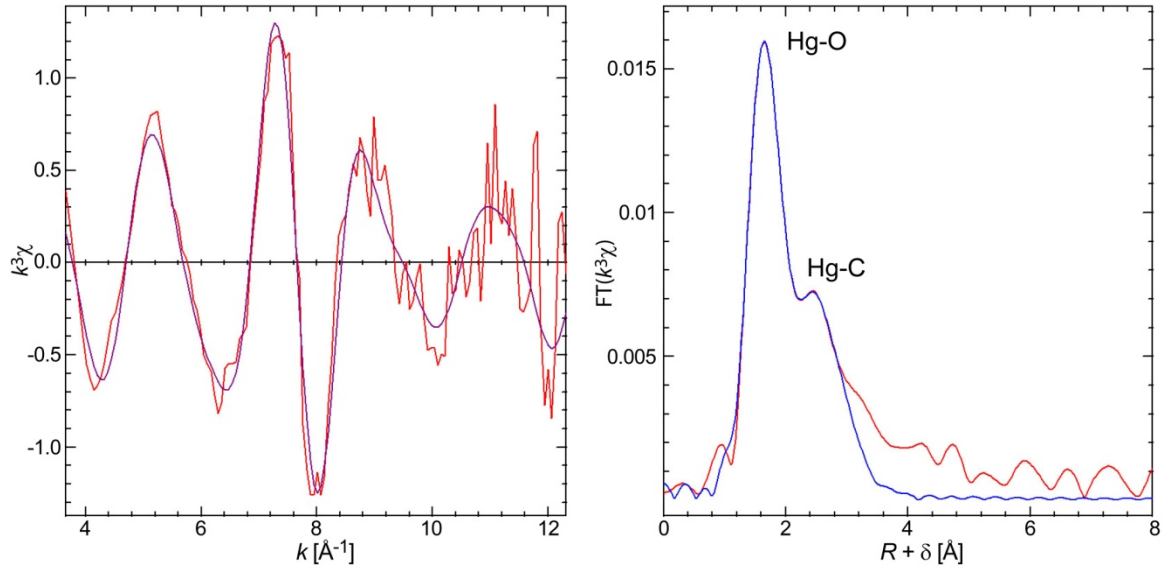

Figure S3r. **2BS-99 - He-T - Model 1.** The best model suggests a five-membered chelate ring. A similar chelate ring model was reported for a monomethyl mercury-humic acid complex.[37] However, the acetate-like bidentate structure[37] has unusually short bonds of 2.66-2.67 Å to C along with bonds of 2.81-2.85 Å to O. This type of structure should have nearly equal Hg-C and Hg-O distances as in methylmercury bonded to tryptophan (2.78 A and 2.83 Å[38]) and acetate dehydrate (2.89 A and 2.94 Å[28]).

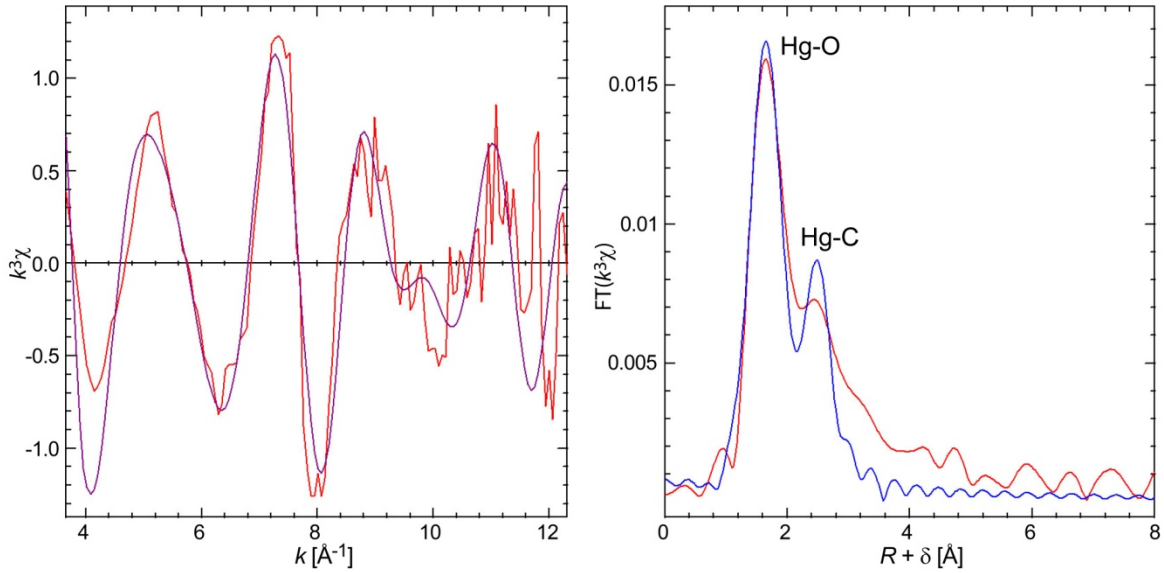

Figure S3s. **2BS-99 - He-T - Model 2.** Considering a linear O-Hg-O complex instead of a five-membered chelate ring structure (with two O shells) decreases the fit quality by more than one order of magnitude.

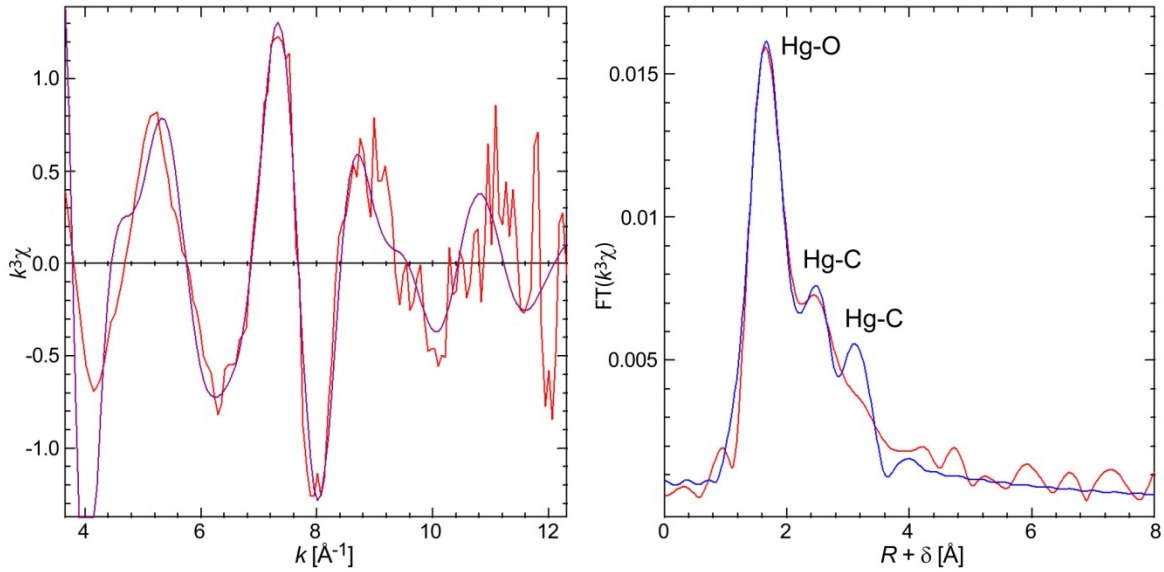

Figure S3t. **2BS-99 - He-T - Model 3.** The fit quality of Model 2 can be restored by allowing σ^2(C) to float, but the fitted value (0.022 Å^2) is meaningless and *CN*(C) is unrealistically high.

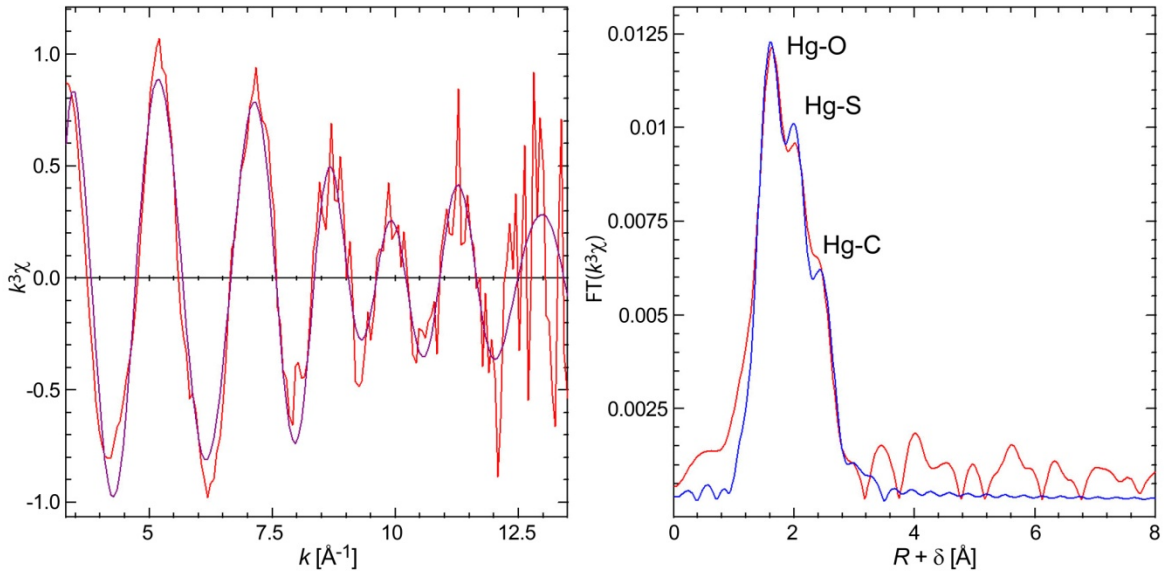

Figure S3u. **F1-99 - RT**. The S shell is detected also at room temperature, but not the second C shell at about 3.3 Å.

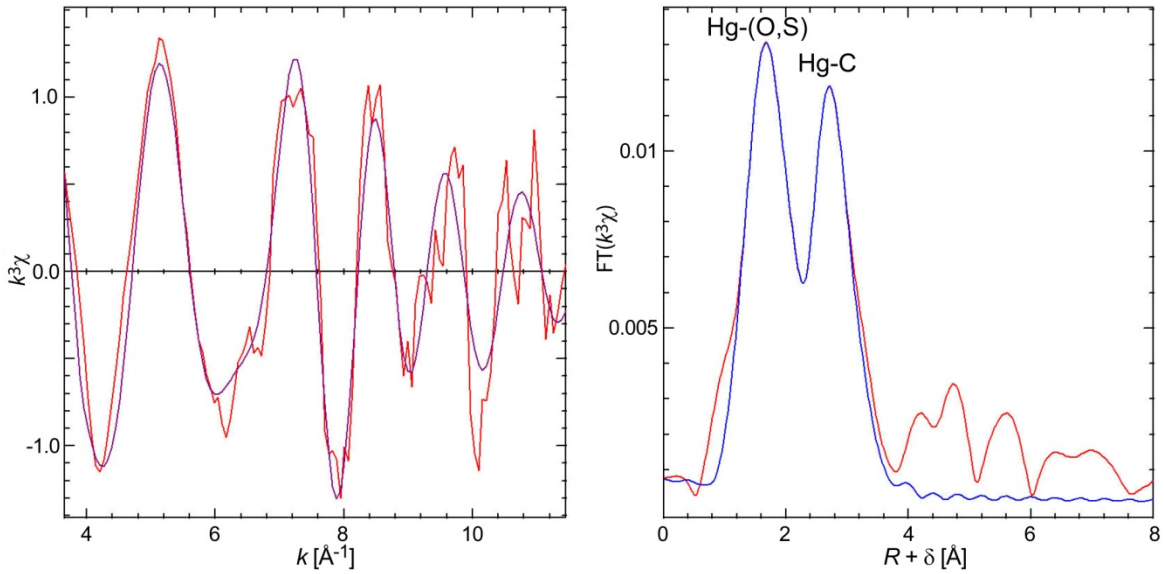

Figure S3v. **F1-99 - He-T - Model 1**

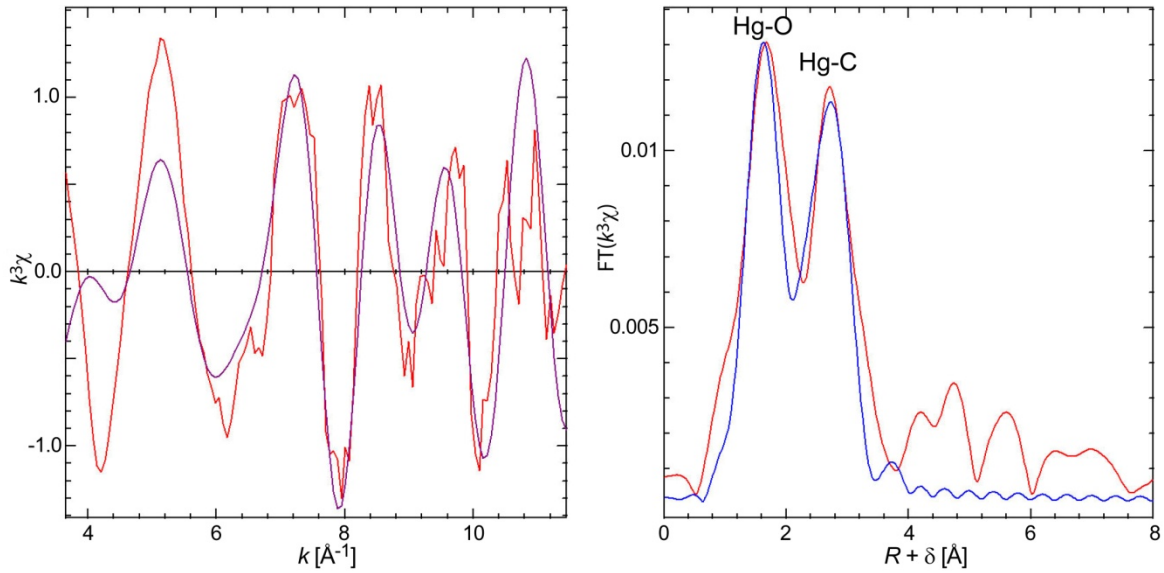

Figure S3w. **F1-99 - He-T - Model 2.** When the S shell is omitted and the σ^2 parameters fixed to their optimal values for 2BS-99 (σ^2(Hg-O)=0.003 Å^2, σ^2(Hg-C)=0.005 Å^2), the fit quality decreases by a factor of 7 because the model fails to reproduce the amplitude, phase and structure of the signal at low *k*.

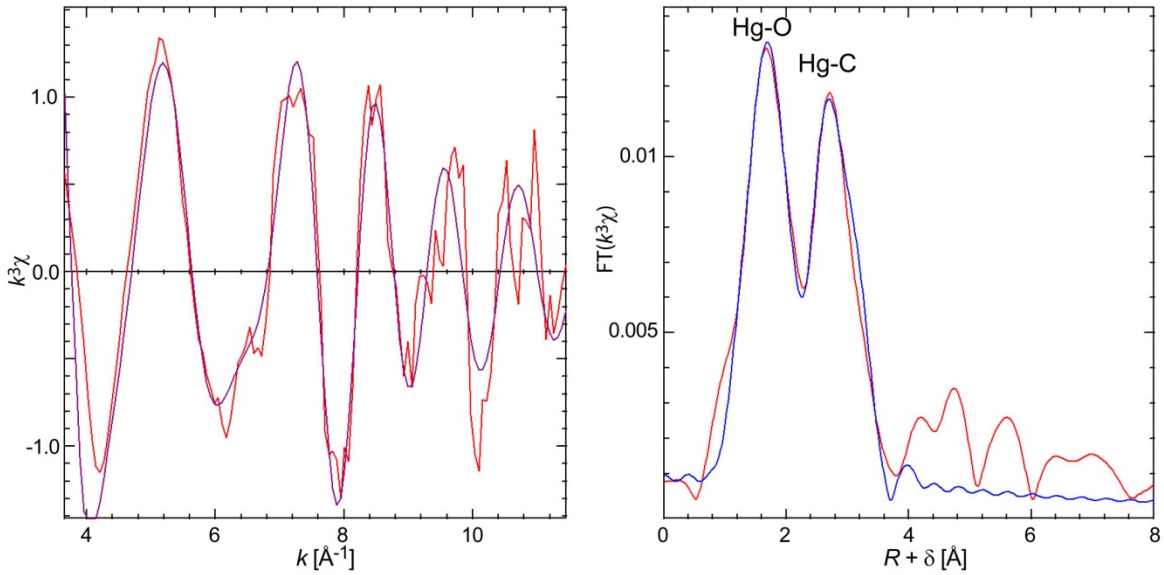

Figure S3x. **F1-99 - He-T - Model 3**. When the S shell is omitted and σ^2 allowed to float, the fit quality is restored but σ^2(Hg-O) and *CN*(C) are too high (Table S3).

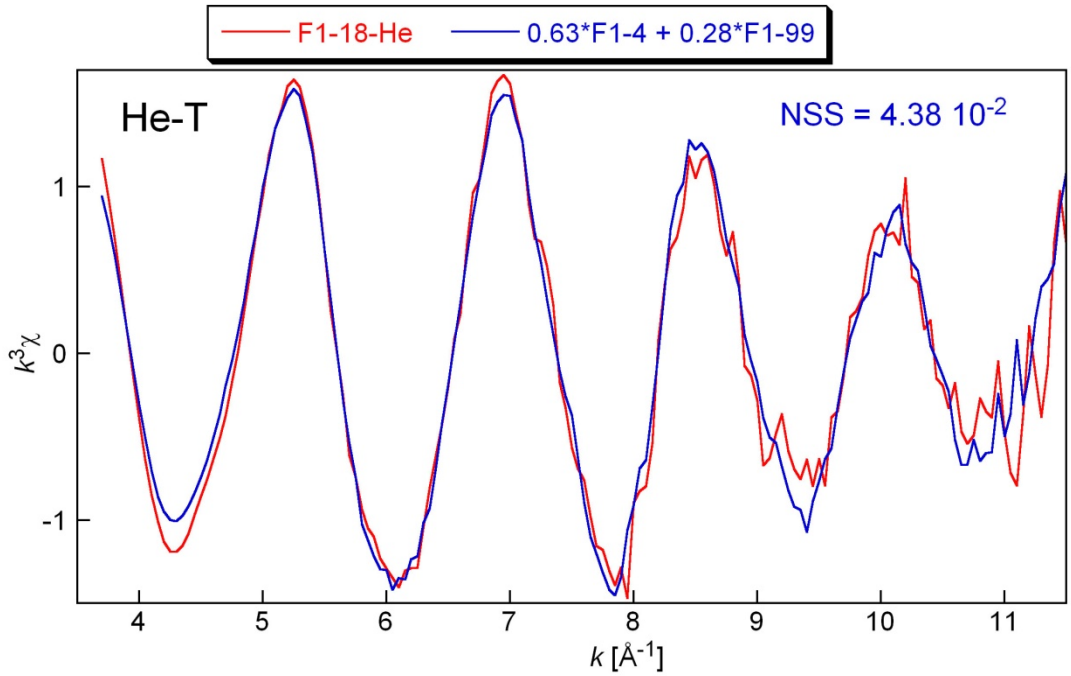

Figure S3y. **F1-18 - He-T.** No fit was attempted because the spectrum is reproduced by a linear combination of F1-4 and F1-99, indicating a mixture of the linear $Hg(SR)_2$ structure with the five-membered chelate ring and the thiolated aromatic environments. The precision on each species is about 10 % total Hg.[39, 40]

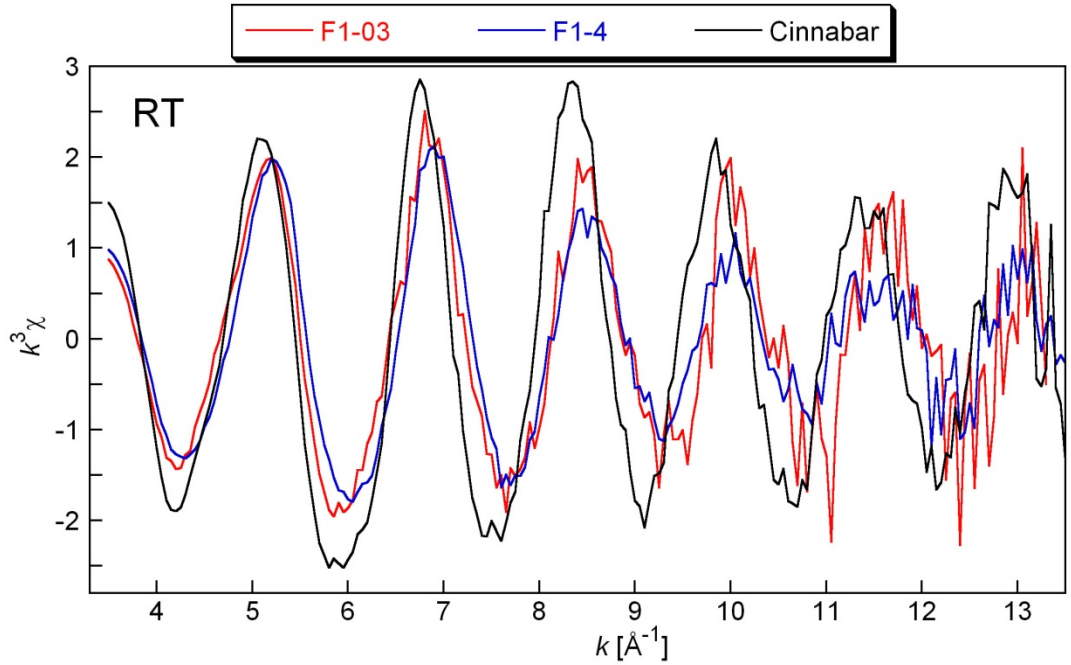

Figure S3z. **RT Spectra for F1-03, F1-4, and Cinnabar.** F1-03 is not a linear combination of the linear $Hg(SR)_2$ and cinnabar structures because its spectral oscillations are not consistently intermediate between those of F1-4 and cinnabar. Note the leftward shift at ~ 4.3-4.6 and ~6.1-6.6 $Å^{-1}$ and the rightward shift above ~9.5 $Å^{-1}$ of F1-03

Table S3. Model parameters from EXAFS least-squares curve-fitting. When several models were tested, the one retained is Fit Model 1.

	T	Fit Model	Hg-O			Hg-S			Hg-C			Hg-Hg			S-Hg-S			ΔE (eV)	$R+\delta$ (Å) window	R_p (%)
			R (Å)	CN	σ^2 (Å^2)	R (Å)	CN	σ^2 (Å^2)	R (Å)	CN	σ^2 (Å^2)	R (Å)	CN	σ^2 (Å^2)	R (Å)	CN	σ^2 (Å^2)			
α-HgS	He-T	1				2.38	2.7	0.004[c]				3.79	5.0	0.006[c]				4.4	1.2-4.9	13.2
						3.07	2.3	0.004[c]				4.11	9.0	0.006[c]						
						3.26	2.4	0.004[c]												
	RT	1				2.38	1.8	0.004				4.14	2.9	0.011				4.8	1.3-4.5	9.1
		2				2.38	1.8[c]	0.004							4.73	1.8[c]	0.009	4.3	1.3-4.5	10.5
β-HgS	He-T	1				2.40	1.2	0.006[c]				4.10	6.5	0.005				0.6	1.3-4.6	14.6
						2.98	1.9	0.006[c]												
						3.19	1.4	0.006[c]												
	RT	1				2.52	3.5	0.010				4.09	1.1	0.011				3.3	1.3-4.3	12.9
Hg(Cys)$_2$	He-T	1				2.32	1.5[c]	0.002	3.31	1.5[c]	0.005				4.64	1.5[c]	0.003	2.9	1.2-4.5	8.0
F1-03	He-T	1				2.34	1.7	0.005[c]	3.25	0.9	0.005[f]	4.12	2.6	0.006				2.5	1.1-4.6	10.1
						2.53	1.3	0.005[c]												
		2[Sk]				2.34	1.7	0.005[c]	3.23	1.0	0.005[f]				4.61	2.2	0.002[n]	0.8		15.2
						2.51	1.3	0.005[c]												
	RT	1				2.35	2.1	0.006[c]				4.14	1.6	0.008				4.3		5.6
						2.57	0.6	0.006[c]												
		2				2.35	2.1	0.005[c]							4.63	0.5	-0.003[n]	3.0		4.2
						2.57	0.6	0.005[c]												
		3				2.35	2.1[c]	0.006[c]							4.63	2.1[c]	0.008[n]	4.6		9.5
						2.57	0.6	0.006[c]												
F1-4	He-T	1	2.01	0.4	0.004[c]	2.33	1.4[c]	0.004[c]							4.61	1.4[c]	0.009	2.3	1.2-4.4	7.0
	RT	1				2.35	2.0	0.009										6.7		5.2

F1-99	He-T	1	2.02	1.0	0.004[c]	2.34	0.4	0.004[c]	2.97	1.7	0.005[c]		2.8	1.0-3.7	2.0
									3.28	4.3	0.005[c]				
		2	2.03	0.8	0.004[f]				2.97	4.8	0.005[f]		-2.0		13.3
									3.21	6.3	0.005[f]				
		3	2.11	4.2	0.019[n]				3.02	8.3[n]	0.010[c]		12.1		2.8
									3.29	9.3[n]	0.010[c]				
	RT	1	2.03	1.0	0.005[c]	2.36	0.4	0.005[c]	2.88	1.0	0.005[c]		7.4	1.1-2.8	5.0
2BS-99	He-T	1	2.02	0.9	0.004[c]				2.87	1.0	0.005[c]		1.7	1.0-3.7	1.0
			2.45	0.6	0.004[c]				3.28	1.4	0.005[c]				
		2	2.05	1.0	0.004[f]				2.86	2.9	0.005[f]		9.0		11.8
									3.15	1.7	0.005[f]				
		3	2.07	0.8	0.008				2.99	11.9[n]	0.022[c,n]		13.0		7.8
									3.27	12.3[n]	0.022[c,n]				
	RT	1	2.03	0.6	0.005[c]				2.85	1.5	0.005[c]		4.1	1.1-3.0	6.1
			2.51	0.7	0.005[c]										
		2	2.04	1.8	0.010				2.88	0.6	-0.002[n]		4.7	1.1-3.0	18

R is bond distance, *CN* is coordination number, σ^2 is the Debye-Waller factor, and ΔE is the shift of the energy threshold *E*0. The uncertainty in *CN*, *R* and σ^2 at the 95% confidence level are about 20 %, 0.02 Å and 0.001 Å^2, respectively. R_p is the fit residual in percent, defined as $\Sigma(|y_{exp}-y_{fit}|)/\Sigma(|y_{exp}|)$. Typical values for R_p are a few percent, indicating that the least-squares refinement is limited by systematic errors in the model calculation. For the same quality of fit, R_p increases with the dimension of the $R + \delta$ fit interval.

[c] correlated to be identical

[f] fixed

[Sk] model of ref 31 [33]

[n] non-physical or non-structural value

S4. Discussion of Cinnabar and Metacinnabar EXAFS Spectra as a Function of Temperature

We reported in the manuscript that the cinnabar spectrum shows more of its crystallographic structure, i.e., longer Hg-S and Hg-Hg bonds, at He-T than at RT because of the reduced thermal motion of its atoms. We also reported that metacinnabar undergoes a structural transformation between RT and He-T that suggests it is approaching the cinnabar crystal structure at low temperature. A structural transformation of metacinnabar at He-T is plausible because it is even further from its stability field than at RT[41]. The transition is from a higher to lower degree of symmetry, similar to the high-to-low symmetry transition reported for magnetite at 125 K.[42] The question remains as to where in temperature space the transition actually occurs. To begin to answer this question we use data from ref 1[1] who measured the EXAFS spectra of cinnabar and metacinnabar at liquid nitrogen temperature (LN_2-T; 77 K).

In Figure S4a, we reproduce Figures S2a and S4a of the SI of ref 1[1] and in the lower part of the figure we show our cinnabar spectrum at He-T The authors fit their spectrum of cinnabar obtained at 77 K as a linear combination of the spectrum of cinnabar at RT and the spectrum of elemental Hg at 77 K, making the assumption that the spectrum of cinnabar would not change between RT and 77 K. The vertical aqua band shows a shoulder in the LN_2-T cinnabar spectrum at k = 7.6 to 8.2 $Å^{-1}$ that cannot be explained by a spectral feature of elemental Hg. The fit shown in the middle part of this figure is poor in this region. The features in the cinnabar spectrum marked with arrows at k ~ 5.9 $Å^{-1}$ and k ~ 9.7 $Å^{-1}$ in their Figure S2a and highlighted in yellow are also not fit well in their Figure S4a (middle plot). We propose that all of the features marked by arrows in their Figure S2s are actually structural features from longer bonds in cinnabar that appear at lower temperature as shown in our Figure S3d and Table S3. Based on this new interpretation, there is no evidence for elemental Hg in cinnabar.

Figure S4b reproduces Figure S2b of ref 1[1] and our metacinnabar spectrum at He-T. Our measured spectrum was corrected by removing 16% of the cinnabar spectrum obtained at He-T based on the 16% cinnabar impurity observed in the XRD pattern of the metacinnabar described in Section S3. We also assume that the top two curves of ref 1[1] have their labels switched and instead follow the order these authors showed for cinnabar (77 K spectrum on top; RT spectrum in the middle; elemental Hg spectrum at 77 K at the bottom) and the order listed in their figure caption. The three arrows in their figure, marked with yellow bands in the composite figure, all align with spectral oscillations in our metacinnabar at He-T. We see a minimum amplitude at the position of the arrow marked with the aqua band, as do these authors. We do not see evidence for the presence of the oscillation at k ~ 7.3 $Å^{-1}$ in elemental Hg. This comparison suggests that metacinnabar has already begun to undergo a structural transition at 77 K. The conclusion that elemental Hg is present in their metacinnabar is ambiguous.

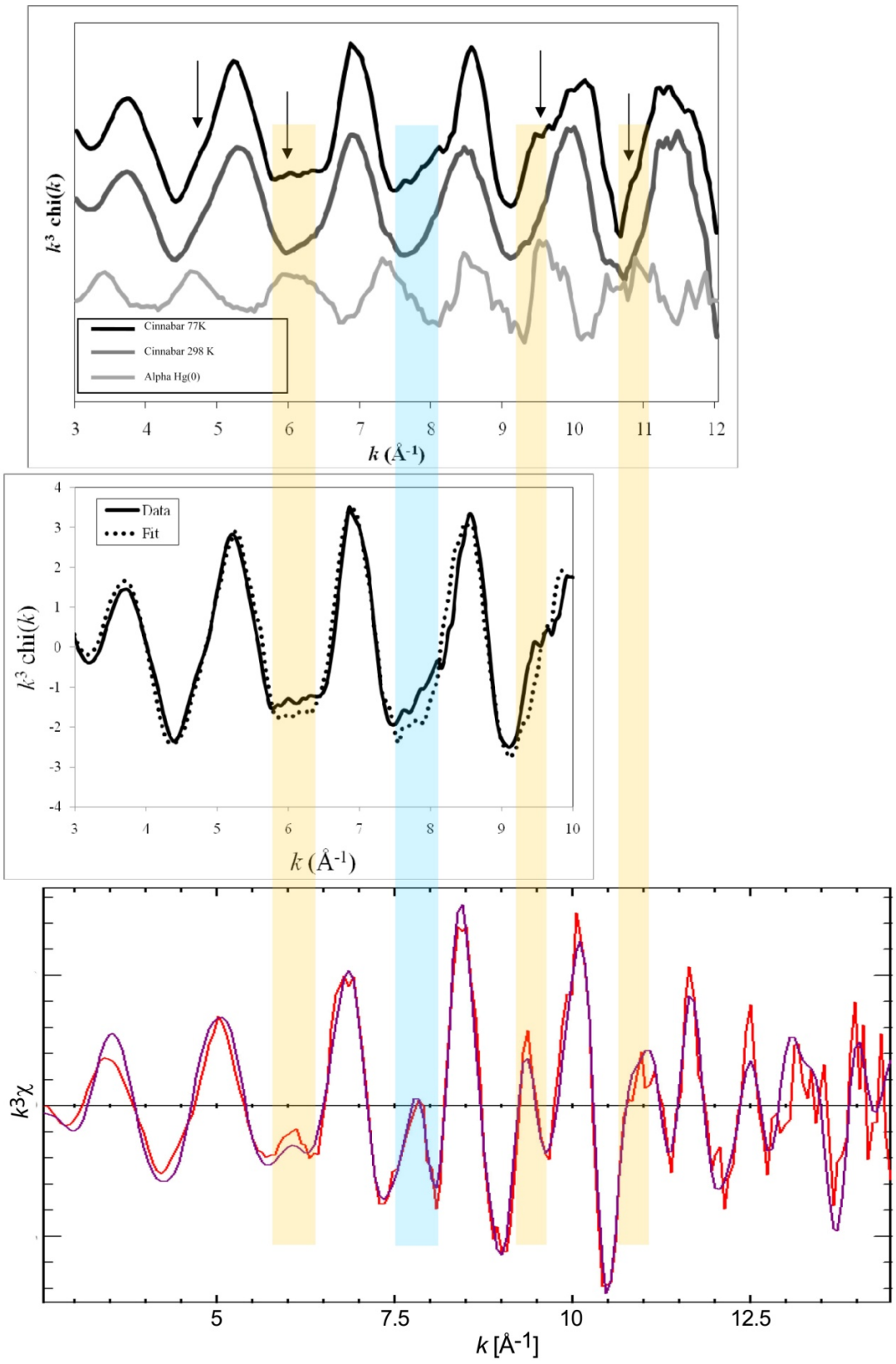

Figure S4a. **Comparison of cinnabar spectra at 77 K[1] and He-T (this study).** The top two figures are taken from ref 1[1] (their Figures S2a and S4a). The bottom figure is our spectrum at He-T (our Figure S3d). The yellow bands match features in their spectra purported to arise from the presence of elemental Hg. These features match cinnabar structural features we observed and modeled at He-T. The aqua band matches a feature in their and our spectra that is absent in their elemental Hg spectrum.

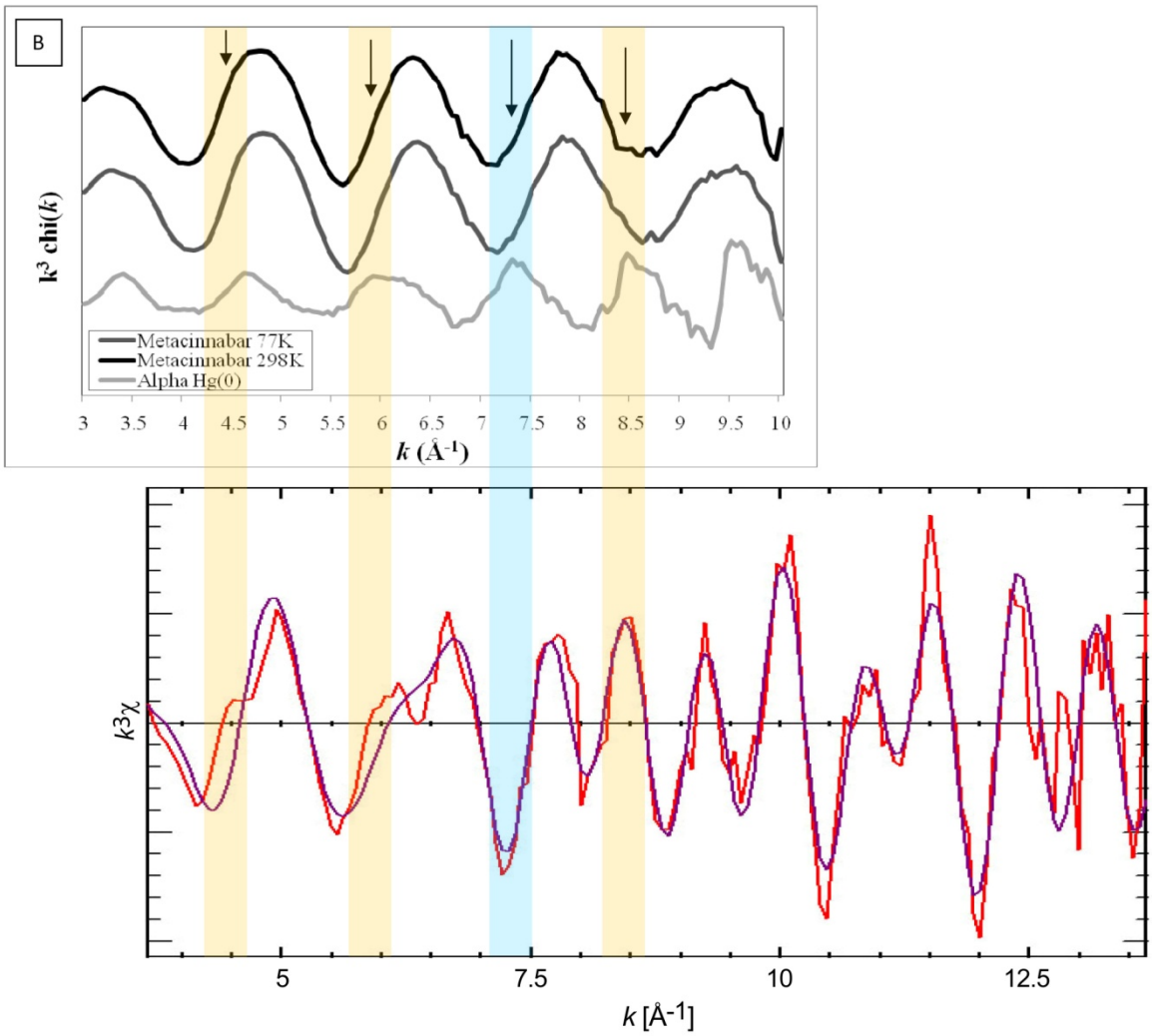

Figure S4b. **Comparison of metacinnabar spectra at 77 K[1] and He-T (this study).** The top figure is taken from ref 1[1] (their Figure S2b). The bottom figure is our spectrum at He-T corrected for the presence of 16 % cinnabar (our Figure S3f). The yellow bands match features in the spectra purported to arise from the presence of elemental Hg. These features match structural features of metacinnabar we observed and modeled at He-T. The aqua band matches amplitude minima in the two metacinnabar spectra (ref 1[1] and this study) that show no contribution from elemental Hg.

S5. References

(1) Jew, A. D.; Kim, C. S.; Rytuba, J. J.; Gustin, M. S.; Brown Jr., G. E., New technique for quantification of elemental Hg in mine wastes and its implications for mercury evasion into the atmosphere. *Environ. Sci. Technol.* **2011,** *45*, 412-417.
(2) Lamborg, C. H.; Tseng, C.-M.; Fitzgerald, W. F.; Balcom, P. H.; Hammerschmidt, C. R., Determination of the mercury complexation characteristics of dissolved organic matter in natural waters with "reducible Hg" titrations. *Environ. Sci. Technol.* **2003,** *37*, 3316-3322.
(3) Drexel, R. T.; Haitzer, M.; Ryan, J. N.; Aiken, G. R.; Nagy, K. L., Mercury(II) sorption to two Florida Everglades peats: Evidence for strong and weak binding and competition by dissolved organic matter released from the peat. *Environ. Sci. Technol.* **2002,** *36*, 4058-4064.
(4) Gilmour, C. C.; Riedel, G. S.; Ederington, M. C.; Bell, J. T.; Gill, G. A.; Stordal, M. A., Methylmercury concentrations and production rates across a trophic gradient in the northern Everglades. *Biogeochemistry* **1998,** *40*, 327-345.
(5) Jensen, J. R.; Rutchey, K.; Koch, M. S.; Narumalini, S., Inland wetland change detection in the Everglades Water Conservation Area 2A using a time series of normalized remotely sensed data. *Photogramm. Eng. Remote Sens.* **1995,** *61*, 199-209.
(6) Hurley, J. P.; Krabbenhoft, D. P.; Cleckner, L. B.; Olson, M. L.; Aiken, G. R.; Rawlik, P. S., System controls on the aqueous distribution of mercury in the northern Florida Everglades. *Biogeochemistry* **1998,** *40*, 293-311.
(7) Vaithiyanathan, P.; Richardson, C. J.; Kavanaugh, R. G.; Craft, C. B.; Barkay, T., Relationships of eutrophication to the distribution of mercury and to the potential for methylmercury production in peat soils of the Everglades. *Environ. Sci. Technol.* **1996,** *30*, 2591-2597.
(8) Cleckner, L. B.; Gilmour, C. C.; Hurley, J. P.; Krabbenhoft, D. P., Mercury methylation in periphyton in the Florida Everglades. *Limnol. Oceanogr.* **1999,** *44*, 1815-1825.
(9) Marcus, M. A.; A., M. A.; Celestre, R.; Manceau, A.; Miller, T.; Padmore, H. A.; Sublett, R. E., Beamline 10.3.2 at ALS: a hard X-ray microprobe for environmental and materials sicences. *J. Synchrotron Radiat.* **2004,** *11*, 239-247.
(10) Manceau, A.; Marcus, M. A.; Tamura, N., Quantitative speciation of heavy metals in soils and sediments by synchrotron X-ray techniques. In *Applications of Synchrotron Radiation in Low-Temperature Geochemistry and Environmental Science*, Fenter, P. A.,Rivers, M. L.,Sturchio, N. C.,Sutton, S. R., Eds. Mineralogical Society of America: Washington, D.C., 2002; Vol. 49, pp 341-428.
(11) Jalilehvand, F., Sulfur: not a 'silent' element any more. *Chem. Soc. Rev.* **2006,** *35*, 1256-1268.
(12) Vairavamurthy, A., Using X-ray absorption to probe sulfur oxidation states in complex molecules. *Spectrochimica Acta* **1998,** *A54*, 2009-2017.
(13) Vairavamurthy, M. A.; Maletic, D.; Wang, S.; Manowitz, B.; Elginton, T.; Lyons, T., Characterization of sulfur-containing functional groups in sedimentary humic substances by X-ray absorption near-edge structure spectroscopy. *Energy and Fuels* **1997,** *11*, 546-553.
(14) Skyllberg, U.; Xia, K.; Bloom, P. R.; Nater, E. A.; Bleam, W. F., Binding of mercury to reduced sulfur in soil organic matter along upland-peat soil transects. *J. Environ. Qual.* **2000,** *29*, 855-865.
(15) Beauchemin, S.; Hesterberg, D.; Beauchemin, M., Principal component analysis approach for modeling sulfur K-XANES spectra of humic acids. *Soil Sci. Soc. Am. J.* **2002,** *66*, 83-91.
(16) Solomon, D.; Lehmann, J.; Lobe, I.; Martinez, C. E.; Tveitnes, S.; Du Preez, C. C.; Amelung, W., Sulphur speciation and biogeochemical cycling in long-term arable cropping of subtropical soils: evidence from wet-chemical reduction and S K-edge XANES spectroscopy. *Eur. J. Soil Sci.* **2005,** *56*, 621.
(17) Zhao, F. J.; Lehmann, J.; Solomon, D.; Fox, M. A.; McGrath, S. P., Sulphur speciation and turnover in soils: evidence from sulphur K-edge XANES spectroscopy and isotope dilution studies. *Soil Biology and Biochemistry* **2006,** *38*, 1000-1007.
(18) Einsiedl, F.; Schäfer, T.; Northrup, P., Combined sulfur K-edge XANES spectroscopy and stable isotope analyses of fulvic acids and groundwater sulfate identify sulfur cycling in a karstic catchment area. *Chem. Geol.* **2007,** *238*, 268-276.
(19) Schroth, A. W.; Bostick, B. C.; Graham, M.; Kaste, J. M.; Mitchell, M. J.; Friedland, A. J., Sulfur species behavior in soil organic matter during decomposition. *J. Geophys. Res.* **2007,** *112*, G04011.
(20) Preitzel, J.; Thieme, J.; Salomé, M.; Knicker, H., Sulfur K-edge XANES spectroscopy reveals differences in sulfur speciatilon of bulk soils, humic acid, fulvic acid, and particle size separates. *Soil Biology and Biochemistry* **2007,** *39*, 877-890.
(21) Casagrande, D. J.; Given, P. H., Geochemistry of amino acids in some Florida peat accumulations-I. Analytical approach and total amino acid concentrations. *Geochim. Cosmochim. Acta* **1974,** *44*, 1493-1507.
(22) Casagrande, D. J.; Gronli, K.; Sutton, N., The distribution of sulfur and organic matter in various fractions of peat: origins of sulfur in coal. *Geochim. Cosmochim. Acta* **1980,** *44*, 25-32.

(23) Proux, O.; Nassif, V.; Prat, A.; Ulrich, O.; Lahera, E.; Biquard, X.; Menthonnex, J. J.; Hazemann, J. L., Feedback system of a liquid-nitrogen-cooled double-crystal monochromator: design and performances. *J. Synchrotron Radiat.* **2006,** *13*, 59-68.
(24) Ressler, T., WinXAS: a program for X-ray absorption spectroscopy data analysis under MS-Windows. *J. Synchrotron Radiat.* **1998,** *5*, 118-122.
(25) Ankudinov, A. L.; Rehr, J. J., Relativistic calculations of spin-dependent X-ray-absorption spectra. *Phys. Rev. B: Condens. Matter Mater. Phys.* **1997,** *56*, 1712-1716.
(26) Bradley, D. C.; Kunchur, N. R., Structures of mercury mercaptides. I. X-ray structural analysis of mercury methylmercaptide. *J. Chem. Phys.* **1964,** *40*, 2258-2261.
(27) Aurivillius, K., An X-ray and neutron diffraction study of metacinnabarite. *Acta. Chem. Scand.* **1964,** *18*, 1552-1553.
(28) Allmann, R., Die struktur des quecksilber(II)-acetats. *Zeitschrift für Kristallography* **1973,** *138*, 366-373.
(29) Bergmann, J.; Kleeberg, R.; Taut, T.; Haase, A., Quantitative phase analysis using a new Rietveld algorithm - assisted by improved stability and convergence behavior. *Advances in X-Ray Analysis* **1997,** *40*, 425-436.
(30) Michalowicz, A.; Provost, K.; Laruelle, S.; Mimouni, A.; Vlaic, G., F-test in EXAFS fitting of structural models. *J. Synchrotron Radiat.* **1999,** *6*, 233-235.
(31) Downward, L.; Booth, C. H.; Lukens, W. W.; Bridge, F. In *A variation of the F-Test for determining statistical relevance of particular parameters in EXAFS fits*, 2007; 2007; pp 129-131.
(32) Manceau, A.; Nagy, K. L., Relationships between Hg(II)-S bond distance and Hg(II) coordination in thiolates. *Dalton Trans.* **2008**, 1421-1425.
(33) Skyllberg, U.; Bloom, P. R.; Qian, J.; Lin, C.-M.; Bleam, W. F., Complexation of mercury(II) in soil organic matter: EXAFS evidence for linear two-coordination with reduced sulfur groups. *Environ. Sci. Technol.* **2006,** *40*, 4174-4180.
(34) Mansour, A. N.; Melendres, C. A., Analysis of X-ray absorption spectra of some nickel oxycompounds using theoretical standards. *The Journal of Physical Chemistry A* **1998,** *102*, 65-81.
(35) Carrera, F.; Sánchez Marcos, E. S.; Merkling, P. J.; Chaboy, J.; Muñoz-Páez, A., Nature of metal binding sites in Cu(II) complexes with histidine and related N-coordinating ligands, as studied by EXAFS. *Inorg. Chem.* **2004,** *43*, 6674-6683.
(36) Penner-Hahn, J. E., Characterization of "spectroscopically quiet" metals in biology. *Coord. Chem. Rev.* **2005,** *249*, 161-177.
(37) Yoon, S.-J.; Diener, L.; Bloom, P. R.; Nater, E. A.; Bleam, W. F., X-ray absorption studies of CH_3Hg^+-binding sites in humic substances. *Geochim. Cosmochim. Acta* **2005,** *69*, 1111-1121.
(38) Corbeil, M.-C.; Beauchamp, A. L., Methylmercury(II) complexes with tryptophan and its N-acetyl derivative. *Can. J. Chem.* **1988,** *66*, 2458-2464.
(39) Isaure, M. P.; Laboudigue, A.; Manceau, A.; Sarret, G.; Tiffreau, C.; Trocellier, P.; Hazemann, J. L.; Chateigner, D., Quantitative Zn speciation in a contaminated dredged sediment by mPIXE, mSXRF, EXAFS spectroscopy and principal component analysis. *Geochim. Cosmochim. Acta* **2002,** *66*, 1549-1567.
(40) Panfili, F.; Manceau, A.; Sarret, G.; Spadini, L.; Kirpichtchikova, T.; Bert, V.; Laboudigue, A.; Marcus, M. A.; Ahamdach, N.; Libert, M. F., The effect of phytostabilization on Zn speciation in a dredged contaminated sediment using scanning electron microscopy, X-ray fluorescence, EXAFS spectroscopy and principal components analysis. *Geochim. Cosmochim. Acta* **2005,** *69*, 2265-2284.
(41) Potter, R. W.; Barnes, H. L., Phase relationsin the binary Hg-S. *Am. Mineral.* **1978,** *63*, 1143-1152.
(42) Kasama, T.; Church, N. S.; Feinberg, J. M.; Dunin-Borkowski, R. E.; Harrison, R. J., Direct observation of ferrimagnetic/ferroelastic domain interactions in magnetite below the Verwey transition. *Earth Planet. Sci. Lett.* **2010,** *297*, 10-17.